remote sensing

MDPI

Article

Cross-Validation of Radio-Frequency-Interference Signature in Satellite Microwave Radiometer Observations over the Ocean

Ying Wu [1,2], Meixin Li [1,2], Yansong Bao [1,2,*] and George P. Petropoulos [3]

[1] Collaborative Innovation Center on Forecast and Evaluation of Meteorological Disasters, Key Laboratory for Aerosol-Cloud-Precipitation of China Meteorological Administration, Nanjing University of Information Science & Technology, Nanjing 210044, China; yingwu@nuist.edu.cn (Y.W.); 20181204011@nuist.edu.cn (M.L.)

[2] School of Atmospheric physics, Nanjing University of Information Science & Technology, Nanjing 210044, China

[3] Department of Geography, Harokopio University of Athens, El. Venizelou 70, Kallithea, 17671 Athens, Greece; gpetropoulos@hua.gr

* Correspondence: ysbao@nuist.edu.cn

Received: 7 September 2020; Accepted: 13 October 2020; Published: 19 October 2020

Abstract: Radio-frequency-interference (RFI) signals have gradually become a more serious problem in active and passive microwave remote sensing. However, currently, there is no reliable RFI source distribution data to evaluate the accuracy of existing RFI identification methods. In this study, a simplified generalized RFI detection method (GRDM) is proposed to detect RFI applied to the ocean surface. Two RFI detection methods, the GRDM and the double-principal component analysis (DPCA) method, are used for cross-validation to obtain RFI recognition thresholds of DPCA in the Advanced Microwave Scanning Radiometer 2 (AMSR2) ocean data. In addition, in the present work the source and distribution characteristics of RFI over the ocean surface are also analyzed. The results show that the proposed scheme can effectively identify RFI signals from AMSR2 data, and only 7.3, 10.65, and 18.7 GHz channels are contaminated by RFI over the ocean surface. There are strong 7.3 GHz interference signals over the waters of East Asia (with the value of ΔTB_H mostly between 5 and 30 K and ΔTBv mostly between 5 and 40 K), Europe (with the value of ΔTB_H mostly between 5 and 40 K and ΔTBv mostly between 5 and 30 K), and North America (with the value of ΔTB_H mostly between 5 and 50 K and ΔTBv mostly between 5 and 30 K). The RFI signals in 10.65 GHz data are mainly distributed over the Mediterranean and other European waters (with the value of ΔTB_H mostly between 5 and 35 K and ΔTBv mostly between 5 and 20 K). The RFI signals at 18.7 GHz are mainly present over the offshore marine areas of North America (with the value of ΔTB_H mostly between 5 and 50 K and ΔTBv mostly between 5 and 40 K), with the strongest RFI distributed near the Great Lakes of America, and the RFI magnitudes over the east and west coasts are stronger than over the south coast. Satellite-borne microwave observations over the ocean suffer from interference mainly from stationary communication/television satellites. Due to the reflection of the sea surface, the range and intensity of RFI are strongly dependent on the relative geometric positions of stationary satellites and space-borne passive instruments. Therefore, RFI coverage area changes every day over the ocean in one 16-day period, which is very different from that over the land.

Keywords: microwave; AMSR2; radio frequency interference; recognition threshold

1. Introduction

Passive thermal radiation received by satellite sensors from a natural Earth–atmosphere system is mixed with artificial signals from the Earth's surface, known as radio frequency interference (RFI). The latter, over the years, has become an increasingly serious problem in active and passive microwave

remote sensing data acquisition [1–3]. Man-made RFI sources come mainly from active microwave emitters built on the ground, such as mobile phones, radar, GPS navigation, air traffic control, and vehicle speed measurement instruments. These RFI sources contaminate the scattering and emission radiation of the Earth's atmosphere and increase unpredictable noise in satellite remote sensing detection [4–6]. Currently, observations from satellite-borne microwave sensors in the C- or X-band are widely used all over the world. Such sensors include the Advanced Microwave Scanning Radiometer–Earth Observing System (AMSR-E) aboard the Aqua satellite [1,2,7,8], the MicroWave Radiation Imager (MWRI) aboard the FY-3 satellite [6], AMSR-E's successor instrument, the Advanced Microwave Scanning Radiometer 2 (AMSR2) [9,10], WindSat, and the Global Precipitation Measurement Microwave Imager (GMI) [11]. Spectral acquisitions from those sensors are contaminated by ground-active microwave emission [12–14], causing the brightness temperature (TB) to be abnormally high compared to the field observation of natural emission and scattered radiation. As a result, the inversion of surface parameters and the analysis of data assimilation have a larger error [15–19]. If the RFI pollution data are not correctly identified and removed, the scientific value of space-borne passive microwave instruments will be significantly reduced [20–23]. To solve this issue, many algorithms have been developed, in which the range and strength of RFI are given quantitatively. Examples include the spectral difference method (SDM) [1], the mean and standard deviation method [2], the principal component analysis (PCA) method [13], the normalized principal component analysis (NPCA) method [6], the double-principal component analysis (DPCA) method [14], and the generalized RFI detection method (GRDM) [9,24].

In 2004, Li et al. first proposed the SDM method to identify RFI in AMSR-E measurements [1]. Njoku et al. (2005) analyzed the RFI pollution in the AMSR-E data and extended their research channel to the C-band and X-band using one-year observation data. The authors pointed out that the mean value and standard deviation of the spectral difference index can be used effectively to identify strong RFI [2]. Li et al. (2006) were the first to propose a PCA approach for land areas, integrating the emission and scattering characteristics of target objects and the correlation between multiple channels of radiometer data into a statistical PCA framework [13]. Zou et al. (2012) used the MWRI data to carry out research on RFI identification on land, and proposed the NPCA method to effectively identify the RFI from snow-covered areas [6]. Zhao et al. (2013) used WindSat observation data to study the RFI recognition algorithm of the sea/ice-covered surface near Greenland and Antarctica [14].

These research studies, amongst other ones, all aimed at detecting the RFI of satellite-borne microwave radiometers on land. Yet, to our knowledge, there is not much research done so far on the identification of RFI over the ocean. Due to the inherently large fluctuation in spectral difference characteristics of the ocean surface, the spectral difference method cannot be applied to the ocean area [13]. Li et al. (2006) proposed the use of a multi-channel regression algorithm, using the measurement correlation between multiple channels and obtained the RFI signal distribution in the WindSat data in European waters [13]. In their study the regression calculation is performed through TB data for a period of time in areas without sea/ice cover and with no RFI signal. In another study, Adams et al. (2010) analyzed the chi-squared (χ^2) test of the inversion product of the ocean area within a certain period of time to reverse the RFI signal in the WindSat data [25]. It was found that the downlink signals of stationary communication/TV satellites reflected from the ocean surface are the main sources of interference with the observations from space-borne passive microwave radiometers over the ocean. The probability estimation algorithm must rely on the inversion of atmospheric parameters, and the probability estimation is carried out for the inverted sea surface parameters. Zabolotskikh et al. (2015) suggested a new technique for the detection of RFI contamination in AMSR2 low-frequency-channel measurements over the ocean. Their method is based both on modeling of AMSR2 TB and on analysis of AMSR2 measurements [26]. Zou et al. (2014) detected RFI resulted by TV signals over oceans from AMSR-E [27]. Tian and Zou (2016) quantitatively calculated the contribution of RFI signals to AMSR2 observations by developing an empirical model [28].

Although the simplified GRDM is evaluated to be a very effective method to detect C-band RFI from AMSR2 over the land, different issues may arise when it is implemented over different surface

types (ocean, ice, snow). Therefore, new coefficients of the GRDM of all AMSR2 channels which are applied to the ocean surface are developed and the use of the proposed approach with AMSR2 data is demonstrated in the present study. Moreover, two independent interference detection methods, namely the GRDM and the DPCA method, are employed for cross-validation and to obtain RFI signals recognition thresholds of the DPCA method on the global ocean surface. In addition, the sources and distribution characteristics of RFI over the ocean is also analyzed.

2. AMSR2 Data

The AMSR2 sensor is an advanced cone-scanning spaceborne microwave radiometer onboard the GCOM-W1 satellite [29]. It has 7-frequency (6.925, 7.3, 10.65, 18.7, 23.8, 36.5, and 89.0 GHz) double polarization (horizontal/vertical) channels. Since the payload AMSR2 of the GCOM-W1 satellite covers exactly the same area every 16 days, the orbital coverage observation range is not the same every day during the 16-day period, and there are certain differences. Moreover, in order to avoid mistaking a snow/ice-covered ocean surface for RFI in winter, only summer L1R TB data are selected, i.e., AMSR2 data acquired from 1 July to 16 July 2019 is used to demonstrate the algorithm use in this study.

3. RFI Detection Methods

Over the ocean, because the microwave emissivity of the sea surface is much lower than that of the land, the sea surface conditions (e.g., wind speed and wind direction) and weather phenomena (e.g., water vapor, precipitation, and clouds) will also cause significant changes in TB, sometimes exceeding the impact of RFI [13]. When the spectral difference method is applied to ocean data, it cannot distinguish between weak RFI signals and weather changes, and there are certain errors in its use. Therefore, in this study, two independent interference detection methods, the GRDM and the DPCA method, are applied to identify RFI over the global ocean surface from AMSR2 low-frequency channel TB data and to perform cross-validation.

3.1. GRDM Method

A simplified GRDM was proposed to recognize C-band RFI, and its effectiveness was validated well by PCA method over the land [9]. Also, it is extended to RFI detection over the ocean in this study. The algorithm is written as Equation (1) [9]:

$$\Delta TB[i] = a_0[i] + \sum_j \left(a_j[i] TB[j] \right) \quad (1)$$

in which $TB[i]$ and $TB[j]$ are AMSR2 TB, i is the index of the detected channel, and j is the index of all the other channels (except the channel at same frequency with different polarization), e.g., 6.925-H, 6.925-V, 7.3-H, 7.3-V, 10.65-H, 10.65-V, 18.7-H, 18.7-V GHz, and so on (i.e., i = 1, 2, 3, 4, 5, 6, 7, 8, and so on). $\Delta TB[i]$ is the $TB[i]$ deviation which is the difference between expected $TB[i]$ value computed using empirically fitted coefficients from all $TB[j]$ and the value of observed $TB[i]$. $a_0[i]$ is the constant term, and $a_j[i]$ are linear regression coefficients. Large values of $\Delta TB[i]$ usually correspond to unnatural emissions from RFI.

The coefficients of the Equation (1) are obtained by linear regression calculation. Then, all the AMSR2 channels have been RFI detected, and the results is that there is no RFI signals are detected at 6.925, 23.8, 36.5, and 89.0 GHz channel over the global ocean. Therefore, channels of interest are those at 7.3, 10.65, and 18.7 GHz. Concrete coefficients developed for ocean surface in Equation (1) are shown in Table 1.

Table 1. Coefficients developed for ocean surface in Equation (1).

Coefficients	ΔTB [i]							
	ΔTB[1] (i = 1)	ΔTB[2] (i = 2)	ΔTB[3] (i = 3)	ΔTB[4] (i = 4)	ΔTB[5] (i = 5)	ΔTB[6] (i = 6)	ΔTB[7] (i = 7)	ΔTB[8] (i = 8)
$a_0[i]$	−3.0385	−2.1317	−7.5344	−6.7285	3.1463	−0.8659	6.9579	12.5611
$a_1[i]$	1	0	−0.0669	0.6068	−0.1435	0.3977	−0.0199	0.0062
$a_2[i]$	0	1	0.8919	0.1550	0.3742	−0.0710	0.0320	0.0322
$a_3[i]$	−0.0567	0.3474	1	0	−0.0139	0.1441	−0.0575	−0.0266
$a_4[i]$	0.8847	0.3084	0	1	0.2023	0.0106	0.1325	0.0613
$a_5[i]$	0.2131	0.8865	−0.0301	0.3797	1	0	0.0161	0.2564
$a_6[i]$	0.0159	−0.4384	0.1141	−0.1579	0	1	0.3029	−0.0003
$a_7[i]$	0.3984	0.3082	0.0001	0.0000	0.1261	0.5499	1	0
$a_8[i]$	−0.1549	−0.1295	0.1459	0.0677	0.9142	0.3147	0	1
$a_9[i]$	−0.9438	−0.7650	0.1827	0.0795	0.4251	0.2049	0.3741	0.8907
$a_{10}[i]$	0.4591	0.3895	−0.1249	−0.0474	−0.5352	−0.3133	0.1404	−0.2832
$a_{11}[i]$	0.4613	0.1383	−0.1138	−0.1184	−0.6113	−0.4222	−0.3277	−0.0305
$a_{12}[i]$	−0.2518	−0.0727	−0.0227	0.0136	0.0703	0.0585	0.5223	0.1948
$a_{13}[i]$	−0.0475	0.0668	0.0653	0.0691	0.1955	0.1380	−0.0369	−0.1535
$a_{14}[i]$	0.0218	−0.0347	−0.0065	−0.0154	−0.0077	−0.0058	−0.1053	0.0055

3.2. DPCA Method

The DPCA method consists of two PCA steps. Taking the RFI detection for the 7.3 GHz horizontal polarization (H-pol) channel as an example, the first PCA step is conducted for the TB vector V consisting of 10 channels. The matrix composed of observation field points for PCA is $\boldsymbol{A}_{10\times \mathrm{N}}$ [14]:

$$\mathrm{V} = \begin{pmatrix} TB7\mathrm{H} \\ TB7\mathrm{V} \\ TB10\mathrm{H} \\ TB10\mathrm{V} \\ TB18\mathrm{H} \\ TB18\mathrm{V} \\ TB23\mathrm{H} \\ TB23\mathrm{V} \\ TB37\mathrm{H} \\ TB37\mathrm{V} \end{pmatrix} \tag{2}$$

$$\boldsymbol{A}_{10\times \mathrm{N}} = \begin{pmatrix} TB7\mathrm{H},1 & TB7\mathrm{H},2 & \cdots & \cdots & TB7\mathrm{H},\mathrm{N} \\ TB7\mathrm{V},1 & TB7\mathrm{V},2 & \cdots & \cdots & TB7\mathrm{V},\mathrm{N} \\ \vdots & \vdots & & & \vdots \\ \vdots & \vdots & & & \vdots \\ TB37\mathrm{V},1 & TB37\mathrm{V},2 & \cdots & \cdots & TB37\mathrm{V},\mathrm{N} \end{pmatrix} \tag{3}$$

where TB is the observed value of AMSR2 TB, subscripts H/V represent horizontal/vertical polarization, the subscript number represents the observed frequency, and N represents the sum of observed pixels.

Construct the covariance matrix of $\boldsymbol{A}$ as:

$$\boldsymbol{R}_{10\times 10} = \boldsymbol{A}\boldsymbol{A}^{\mathrm{T}} \tag{4}$$

Its eigenvalue λ_i (i = 1, 2, … , 10) and eigenvector $\vec{e}_i = [e_{1,i},\ e_{2,i},\ \ldots,\ e_{10,i}]^{\mathrm{T}}$ satisfy:

$$\mathbf{R}\vec{e}_i = \lambda_i \vec{e}_i \ (i = 1,\ 2,\ \ldots,\ 10) \tag{5}$$

where $\vec{e}_i$ represents the ith principal component (PC) and λ_i is the contribution of the ith PC to the total variance.

Project matrix $\boldsymbol{A}$ into the orthogonal space constructed by eigenvectors ($\vec{e}_1, \vec{e}_2, \ldots, \vec{e}_{10}$) to obtain the PC coefficients:

$$\boldsymbol{U}_{10\times N} = \boldsymbol{E}^{\mathrm{T}}\boldsymbol{A} = \begin{pmatrix} \vec{u}_1 \\ \vec{u}_2 \\ \vdots \\ \vec{u}_{10} \end{pmatrix} \tag{6}$$

where $\vec{u}_i = [u_{i,1}, u_{i,2}, \ldots, u_{i,N}]$ ($i = 1, 2, \ldots, 10$) represents the coefficient of the ith PC. Therefore, $\boldsymbol{A}$ can be expressed using $\vec{e}_i$ and the PC coefficient $\vec{u}_i$:

$$\boldsymbol{A} = \sum_{i=1}^{10} \vec{e}_i \vec{u}_i. \tag{7}$$

Based on the PC and PC coefficient, matrix $\boldsymbol{A}$ can be reconstructed into two parts $\boldsymbol{A}_1$ and $\boldsymbol{A}_2$:

$$\boldsymbol{A} = \boldsymbol{A}_1 + \boldsymbol{A}_2 \tag{8}$$

$$\boldsymbol{A}_1 = \sum_{i=1}^{\alpha} \vec{e}_i \vec{u}_i \tag{9}$$

$$\boldsymbol{A}_2 = \sum_{i=\alpha+1}^{10} \vec{e}_i \vec{u}_i \tag{10}$$

where α is an integer constant, the value of which depends on the situation. Since the radiation observations from the natural Earth–atmosphere are highly correlated with the channels, the correlation of the observations between channels is captured by the first several principal components, namely $\boldsymbol{A}_1$. Matrix $\boldsymbol{A}_2$ is the sum of TB from the (α + 1)th to the 10th PC, which is referred to as the residual data matrix. RFI only makes the observed value of the interfered channel abnormally high and is not related to other channels. Therefore, the RFI signal is contained in the residual matrix $\boldsymbol{A}_2$, and α is taken as 3 in this study.

The second PCA step expands the residual matrix $\boldsymbol{A}_2$; that is, it performs NPCA on $\boldsymbol{A}_2$. For example, the RFI detection in the 7.3 GHz H-pol channel:

$$\mathbf{R}^{\mathrm{A}_2}_{\mathrm{indices7H}} = \begin{pmatrix} \frac{TB_{7\mathrm{H}} - TB_{10\mathrm{H}} - \mu_{7\mathrm{H}}}{\sigma_{7\mathrm{H}}} \\ \frac{TB_{10\mathrm{H}} - TB_{18\mathrm{H}} - \mu_{10\mathrm{H}}}{\sigma_{10\mathrm{H}}} \\ \frac{TB_{10\mathrm{V}} - TB_{18\mathrm{V}} - \mu_{10\mathrm{V}}}{\sigma_{10\mathrm{V}}} \\ \frac{TB_{18\mathrm{H}} - TB_{23\mathrm{H}} - \mu_{18\mathrm{H}}}{\sigma_{18\mathrm{H}}} \\ \frac{TB_{18\mathrm{V}} - TB_{23\mathrm{V}} - \mu_{18\mathrm{V}}}{\sigma_{18\mathrm{V}}} \end{pmatrix}_{\mathrm{A}_2} \tag{11}$$

where μ and σ are the mean values and standard deviations of five RFI factors for each field of view.

Similarly, RFI indices for the 7.3 GHz vertical polarization (V-pol) channel, 10.65 GHz H/V-pol channels, and the 18.7 GHz H/V-pol channels ($\mathbf{R}^{A_2}_{\text{indices7V}}$, $\mathbf{R}^{A_2}_{\text{indices10H}}$/$\mathbf{R}^{A_2}_{\text{indices10V}}$, and $\mathbf{R}^{A_2}_{\text{indices18H}}$/$\mathbf{R}^{A_2}_{\text{indices18V}}$) are constructed as follows:

$$\mathbf{R}^{A_2}_{\text{indices7V}} = \begin{pmatrix} \frac{TB_{7V}-TB_{10V}-\mu_{7V}}{\sigma_{7V}} \\ \frac{TB_{10H}-TB_{18H}-\mu_{10H}}{\sigma_{10H}} \\ \frac{TB_{10V}-TB_{18V}-\mu_{10V}}{\sigma_{10V}} \\ \frac{TB_{18H}-TB_{23H}-\mu_{18H}}{\sigma_{18H}} \\ \frac{TB_{18V}-TB_{23V}-\mu_{18V}}{\sigma_{18V}} \end{pmatrix}_{A_2} \tag{12}$$

$$\mathbf{R}^{A_2}_{\text{indices10V}} = \begin{pmatrix} \frac{TB_{10V}-TB_{18V}-\mu_{10V}}{\sigma_{10V}} \\ \frac{TB_{18H}-TB_{23H}-\mu_{18H}}{\sigma_{18H}} \\ \frac{TB_{18V}-TB_{23V}-\mu_{18V}}{\sigma_{18V}} \\ \frac{TB_{23H}-TB_{37H}-\mu_{23H}}{\sigma_{23H}} \\ \frac{TB_{23V}-TB_{37V}-\mu_{23V}}{\sigma_{23V}} \end{pmatrix}_{A_2} \tag{13}$$

$$\mathbf{R}^{A_2}_{\text{indices18H}} = \begin{pmatrix} \frac{TB_{18H}-TB_{23H}-\mu_{18H}}{\sigma_{18H}} \\ \frac{TB_{7H}-TB_{10H}-\mu_{7H}}{\sigma_{7H}} \\ \frac{TB_{7V}-TB_{10V}-\mu_{7V}}{\sigma_{7V}} \\ \frac{TB_{23H}-TB_{37H}-\mu_{23H}}{\sigma_{23H}} \\ \frac{TB_{23V}-TB_{37V}-\mu_{23V}}{\sigma_{23V}} \end{pmatrix}_{A_2} \tag{14}$$

$$\mathbf{R}^{A_2}_{\text{indices18V}} = \begin{pmatrix} \frac{TB_{18V}-TB_{23V}-\mu_{18V}}{\sigma_{18v}} \\ \frac{TB_{7H}-TB_{10H}-\mu_{7H}}{\sigma_{7H}} \\ \frac{TB_{7V}-TB_{10V}-\mu_{7V}}{\sigma_{7V}} \\ \frac{TB_{23H}-TB_{37H}-\mu_{23H}}{\sigma_{23H}} \\ \frac{TB_{23V}-TB_{37V}-\mu_{23V}}{\sigma_{23V}} \end{pmatrix}_{A_2} \tag{15}$$

Actually, both the first and the second step in DPCA method depends on the particular channel that is tested for RFI, which means that the two step is performed for a specific channel that is to be tested with regard to its RFI contamination. For RFI detection at 7.3, 10.65 and 18.7 GHz channels, the first steps in DPCA method, i.e., from Equation (2) to Equation (10), are the same, so the first step for these three-frequency channels only needs to be done once, the second steps (Equations (11)–(15)) are different.

Then, the data matrix $\boldsymbol{B}_{5\times N}$ is reconstructed from $\mathbf{R}^{A_2}_{\text{indices7H}}$:

$$\boldsymbol{B} = \boldsymbol{EU} = \sum_{i=1}^{5} \vec{e}_i \vec{u}_i \tag{16}$$

The eigenvalue vector is expressed as the PC $\vec{e}_1$, $\vec{e}_2$, …, $\vec{e}_5$, and $\vec{u}_i = [u_{i,1}, u_{i,2}, \ldots, u_{i,N}]$ represents the coefficient of the ith PC. A large value of u_1 which is the coefficient value of the first PC of matrix $\boldsymbol{A}_2$ indicates the existence of RFI, and the larger the coefficient value of the first PC, the greater possibility of the existence of a strong RFI.

4. Results

4.1. RFI Detection by GRDM

According to Equation (1) and the coefficients in Table 1, the generalized RFI indices ($\Delta Tb[i]$) in Equation (1) for 6.925, 7.3, 10.65, and 18.7 GHz H-pol channels were obtained. As shown in the results, almost no RFI signal is detected in the observations of the 6.925, 23.8, 36.5, and 89.0 GHz channel over the global ocean (pictures omitted). The RFI signals detected in the 7.3 GHz channel are mainly distributed over the waters of East Asia, Europe, and North America. The RFI signals detected in the 10.65 GHz channel are distributed mainly over European waters. RFI signals detected in the 18.7 GHz channel are mainly distributed over North American waters.

Figures 1–3 present the spatial distribution of 7.3 GHz-H RFI obtained by the GRDM over East Asian, European, and North American waters from 1 July to 16 July 2019. It can be seen from the figures that the greater the ΔTb, the warmer the tones, the greater the probability of RFI and the stronger the intensity. Moreover, RFI generally appeared in a long, narrow strip, but the exact location and the length of the strip, and the strength of the RFI vary from day to day.

Figure 1 illustrates the RFI signals in AMSR2 measurements for H-pol channels of 7.3 GHz over East Asian waters during 16 different days. On 1, 2, 5, 10, and 14 July, the detected RFI over East Asian waters is weak. And on 3, 4, 6, 7, 8, 9, 11, 12, 13, and 15 July, the detected RFI is much stronger, while on 16 July, almost no obvious RFI signal is detected.

Figure 2 depicts the RFI signals in AMSR2 measurements for H-pol channels of 7.3 GHz over European waters during 16 different days. In general, the RFI strip has a northeast–southwest trend: for example, the North Sea–the English Channel–the Bay of Biscay (2, 4, 6, 9, 11, and 13 July), Adriatic Sea–Tyrrhenian Sea (2 July), the North Sea–the Gulf of Lion (3 July), the western waters of Corsica and Sardinia (5 July), the Irish sea to St. George's Channel and Bristol Bay (7 and 16 July), and the North Sea (8 and 15 July). Meanwhile, no significant RFI was detected on 12 or 14 July.

Figure 3 shows the RFI signals in AMSR2 measurements for H-pol channels of 7.3 GHz over North American waters during 16 different days (1–16 July 2019). During the 16 days, almost no RFI signal is detected except on 1, 3, 5, 8, 13, and 15 July. RFI signals of different intensities are detected in the remaining 10 days. The longitude range of the RFI strip is usually between 140° W and 153° W, while the latitude range is usually between 25° N and 37° N.

Figure 4 shows RFI signals in AMSR2 measurements for H-pol channels of 10.65 GHz over European waters on 16 different days. As can be observed in Figure 4, the RFI signals detected over the global ocean surface in the AMSR2 10.65 GHz channel are strongest over European waters. The RFI signals focus mainly on the North Sea, the English Channel, the Bay of Biscay, the Strait of Gibraltar, the Baltic Sea, the Mediterranean, the Black Sea and the Caspian Sea. Similarly, RFI in the AMSR2 10.65 GHz channel also generally appears in a long and narrow strip, while the location and the length of the strip and the strength of the RFI vary every day during the 16 different days. For example, North Sea–St. George's Channel–Bristol Bay–Atlantic Ocean (1, 10 July), Baltic Sea–Ligurian Sea–Mediterranean (1, 10 July), Black Sea–Levantine Sea (1, 10 July), North Sea–Alboran Sea (2 July), Baltic Sea–Adriatic Sea–Ionian Sea (2 July), Black Sea (2, 4, 9, 11, 13, 16 July), North Sea–St George's Channel–Bristol Bay–Atlantic Ocean (3 July), Baltic Sea–Adriatic Sea–Tyrrhenian Sea (3, 5, 6, 7, 12, 14, 16 July), North Sea–Skagerrak–Balearic Sea–Alboran Sea (4, 6, 13, 15 July), Ionian Sea (4 July), North Sea–English Channel–Bay of Biscay–Strait of Gibraltar (5, 7, 14 July), in the southwest seas of the island of Briton and Ireland (8, 13, 15 July), Skagerrak Strait–Ligurian Sea–Balearic Sea (8 July), North Sea–Strait of Dover–Bay of Biscay–Strait of Gibraltar (9, 16 July), Baltic Sea–Adriatic Sea–Ionian Sea (9 July), Caspian Sea (10 July), North Sea–Balearic Sea (11 July), Strait of Otranto–Ionian Sea (11 July), North Sea–Bristol Bay–English Channel–Bay of Biscay–Atlantic Ocean (12 July).

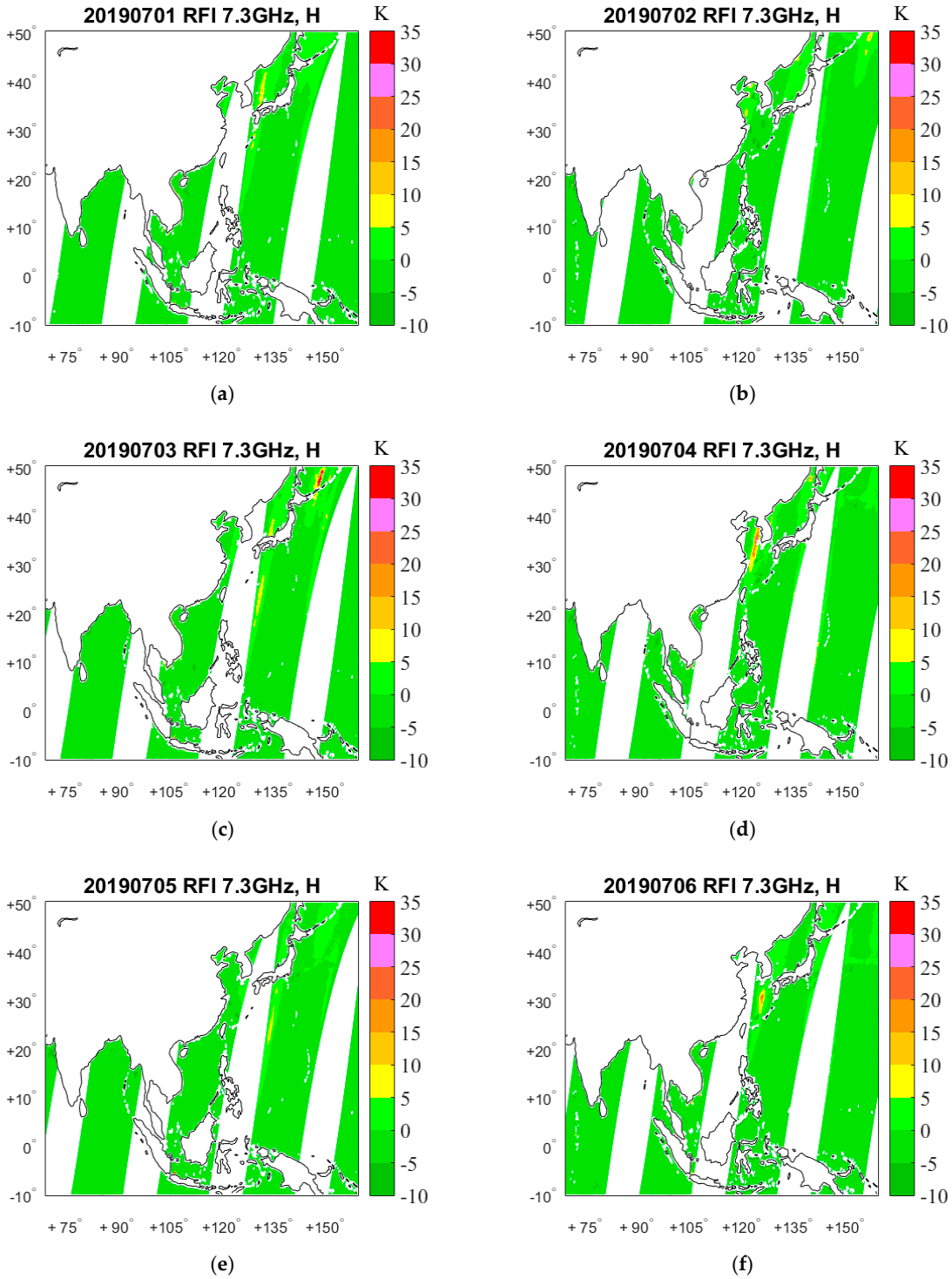

Figure 1. *Cont.*

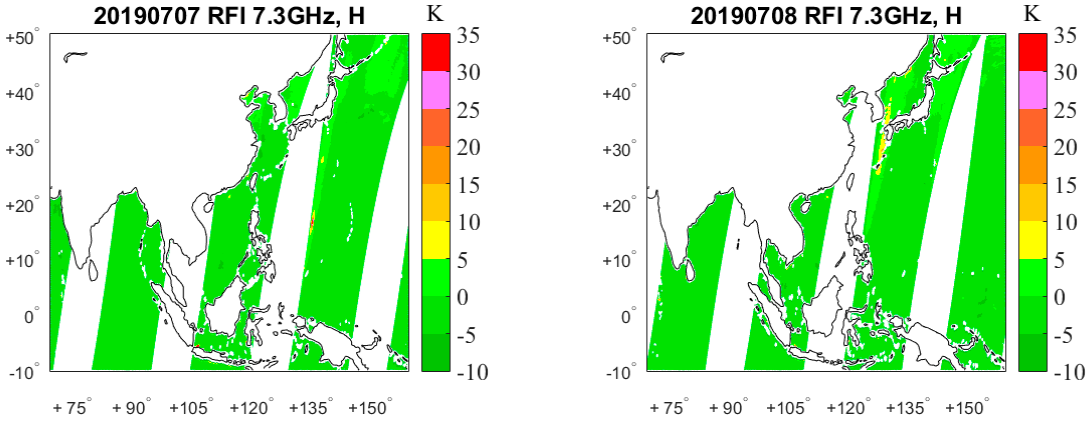

(**g**)

(**h**)

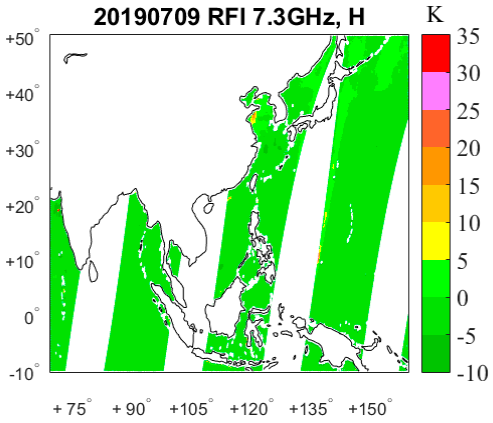

(**i**)

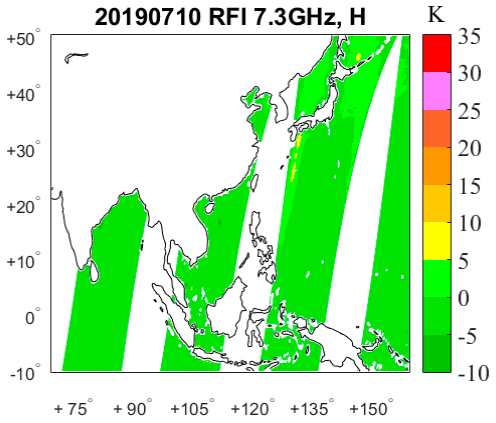

(**j**)

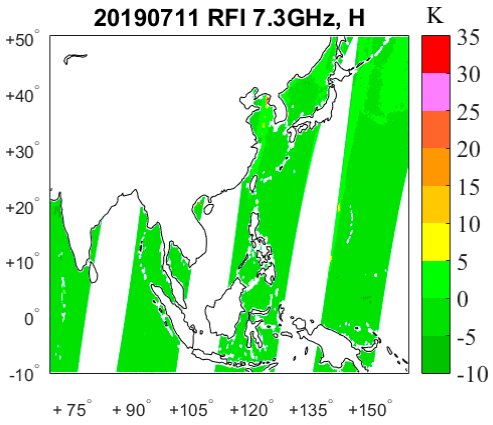

(**k**)

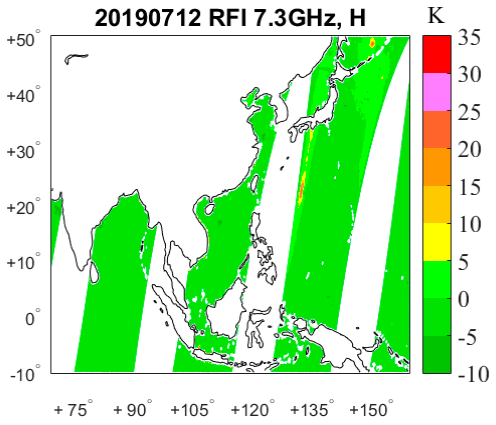

(**l**)

Figure 1. *Cont.*

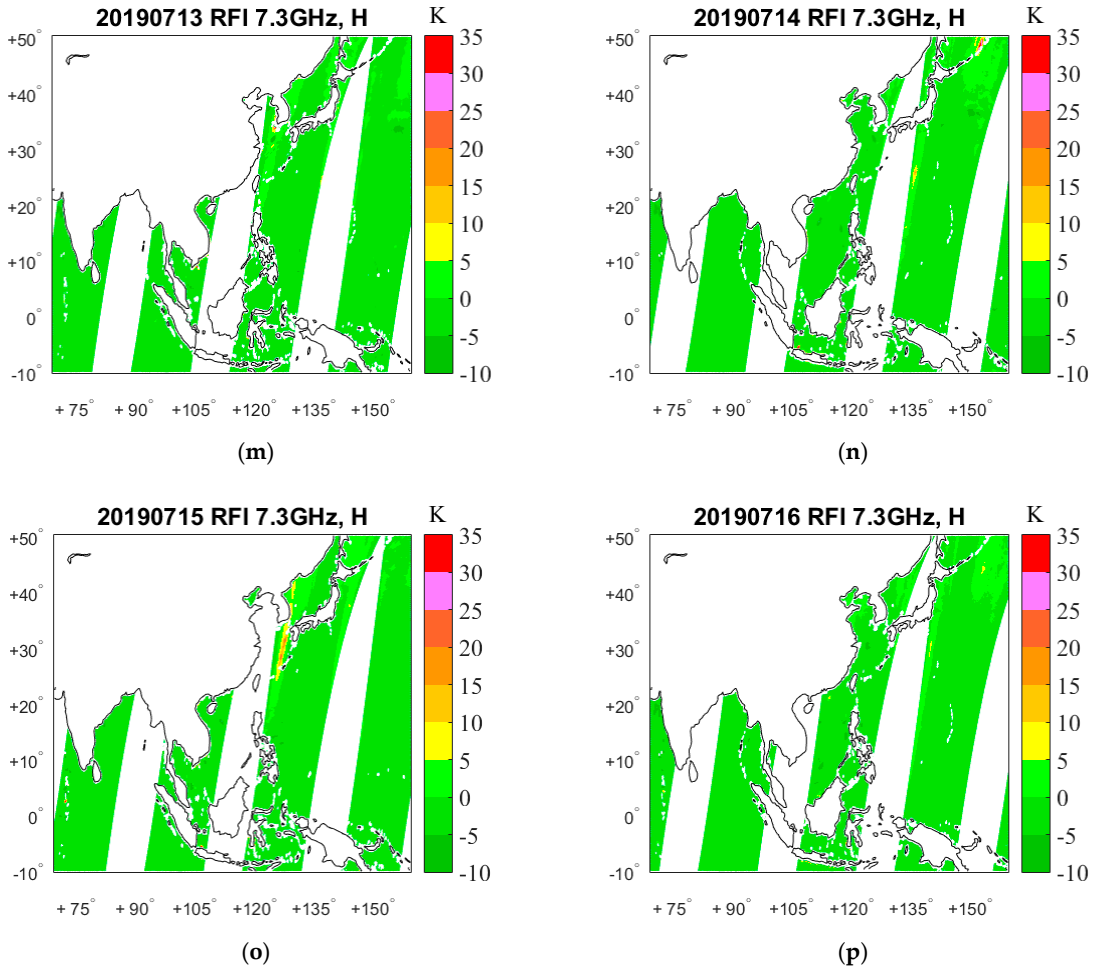

Figure 1. Spatial distribution of 7.3 GHz-H RFI, using GRDM over East Asian waters during the period 1–16 July 2019. (**a**) 1 July; (**b**) 2 July; (**c**) 3 July; (**d**) 4 July; (**e**) 5 July; (**f**) 6 July; (**g**) 7 July; (**h**) 8 July; (**i**) 9 July; (**j**) 10 July; (**k**) 11 July; (**l**) 12 July; (**m**) 13 July; (**n**) 14 July; (**o**) 15 July; (**p**) 16 July.

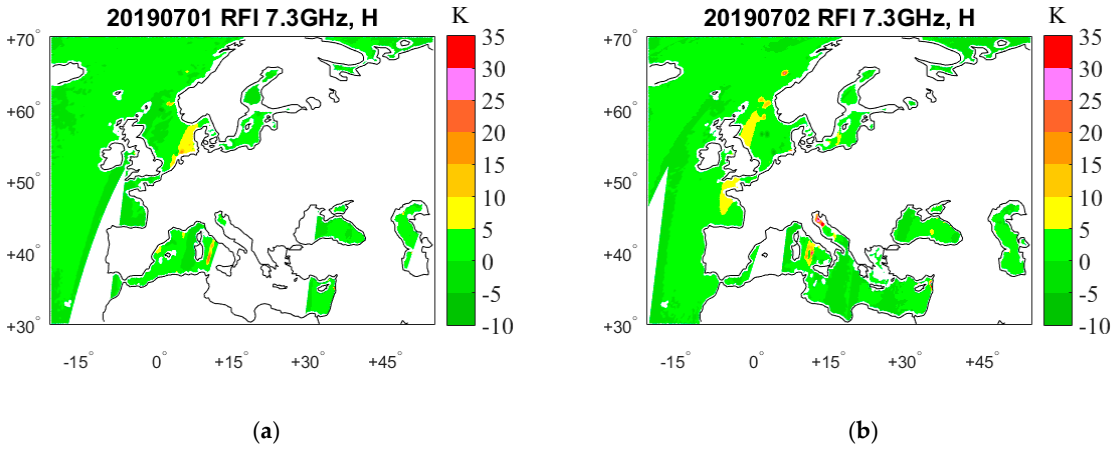

Figure 2. *Cont.*

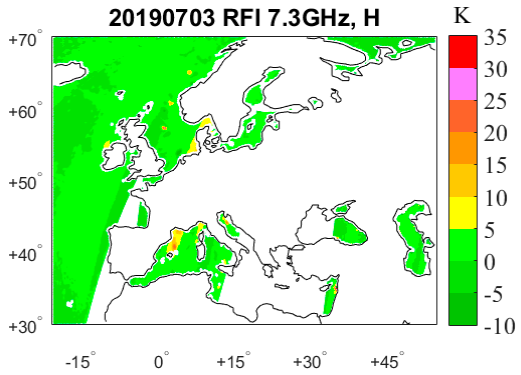

(**c**)

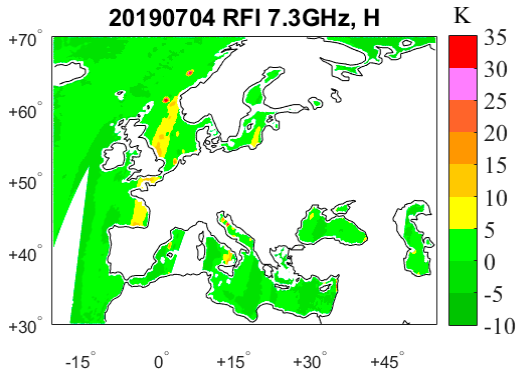

(**d**)

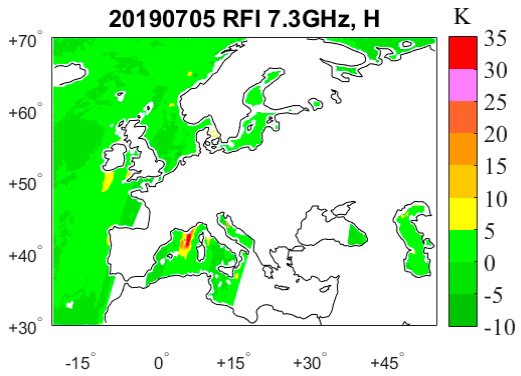

(**e**)

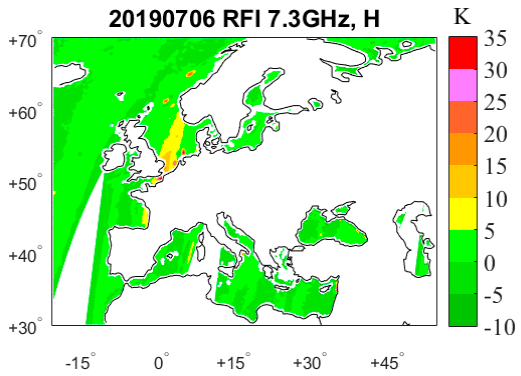

(**f**)

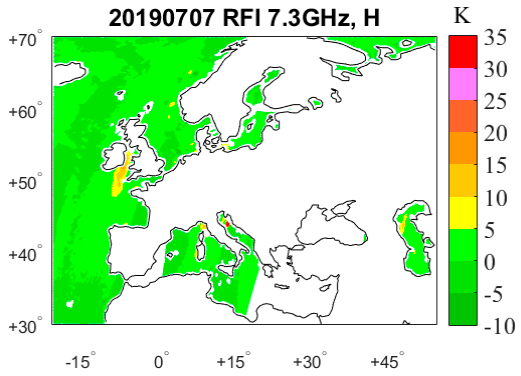

(**g**)

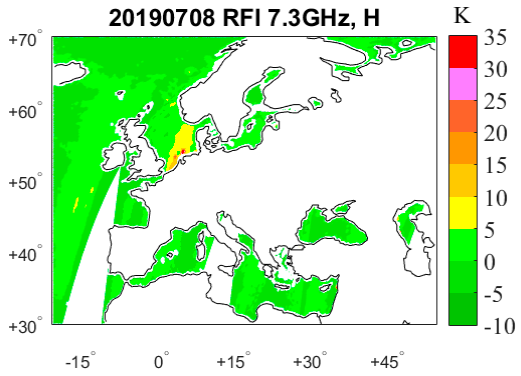

(**h**)

Figure 2. *Cont.*

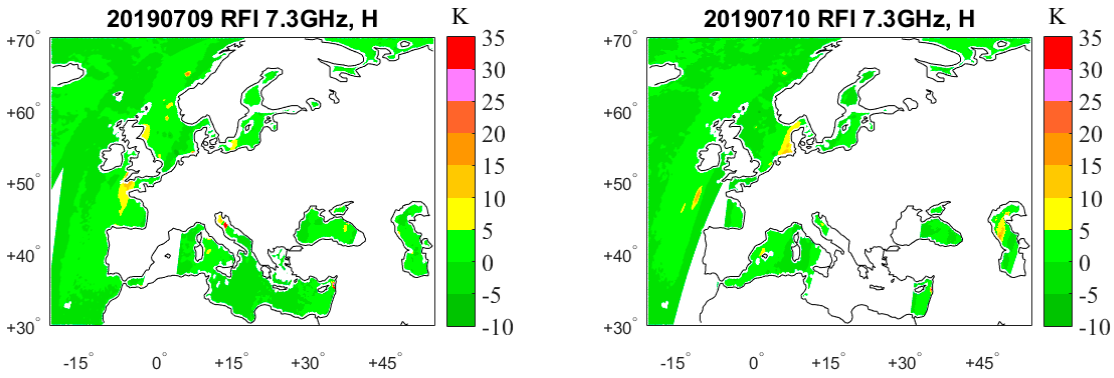

(**i**)

(**j**)

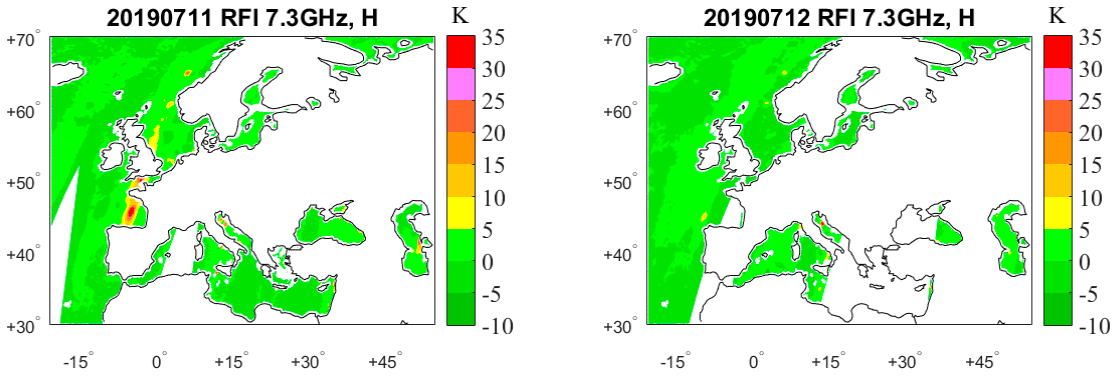

(**k**)

(**l**)

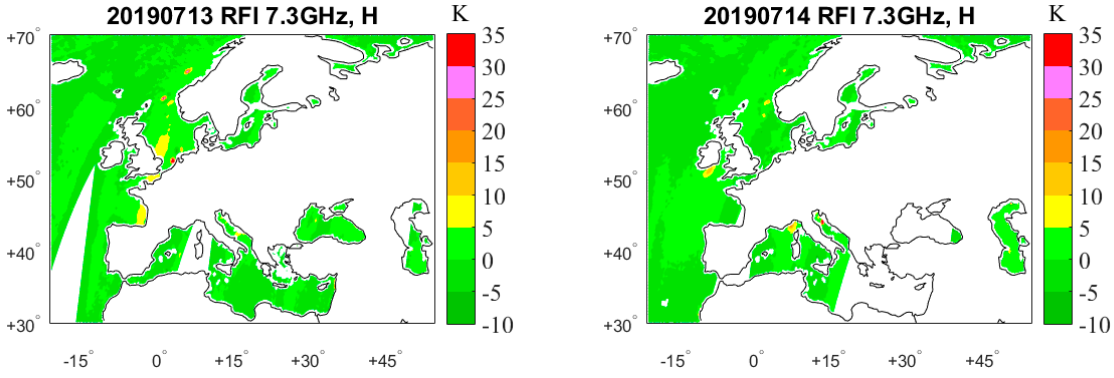

(**m**)

(**n**)

Figure 2. *Cont.*

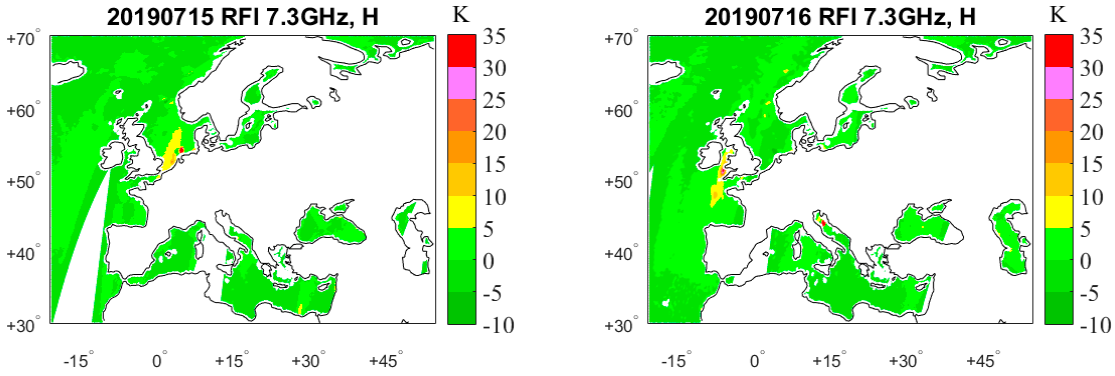

(**o**) (**p**)

Figure 2. Spatial distribution of 7.3 GHz-H RFI, using GRDM over European waters during the period 1–16 July 2019. (**a**) 1 July; (**b**) 2 July; (**c**) 3 July; (**d**) 4 July; (**e**) 5 July; (**f**) 6 July; (**g**) 7 July; (**h**) 8 July; (**i**) 9 July; (**j**) 10 July; (**k**) 11 July; (**l**) 12 July; (**m**) 13 July; (**n**) 14 July; (**o**) 15 July; (**p**) 16 July.

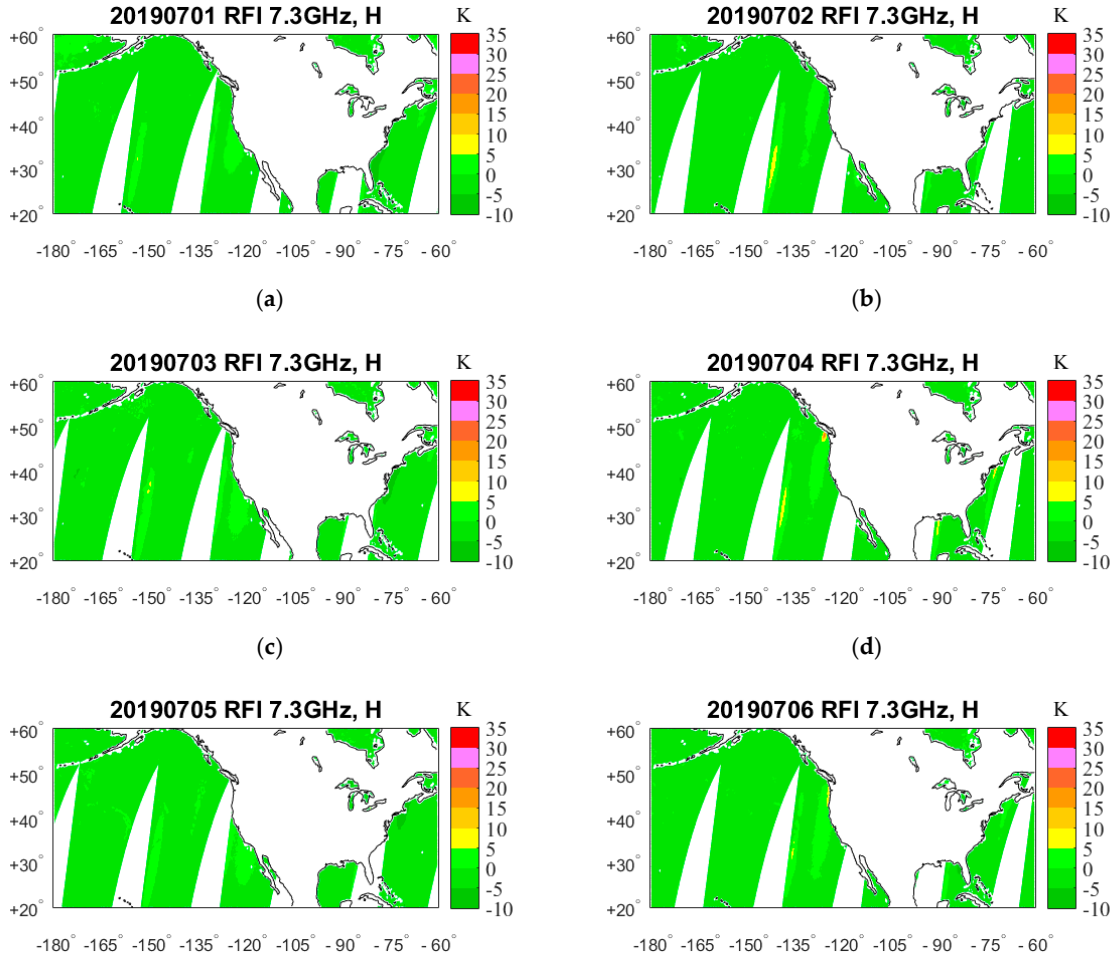

(**a**) (**b**)

(**c**) (**d**)

(**e**) (**f**)

Figure 3. *Cont.*

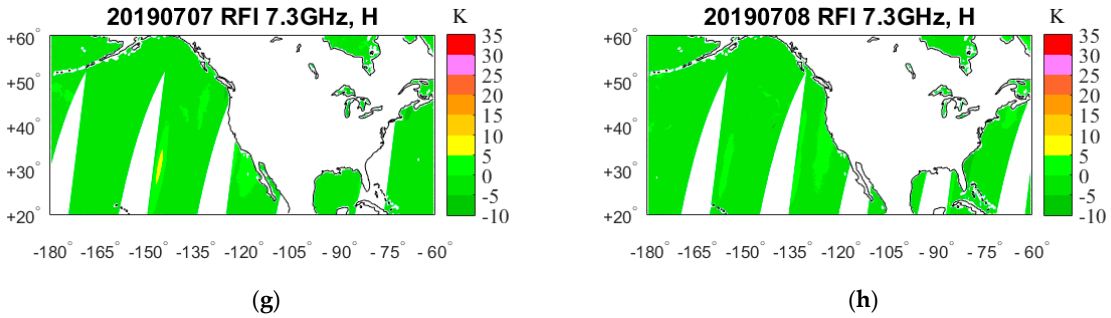

(**g**)

(**h**)

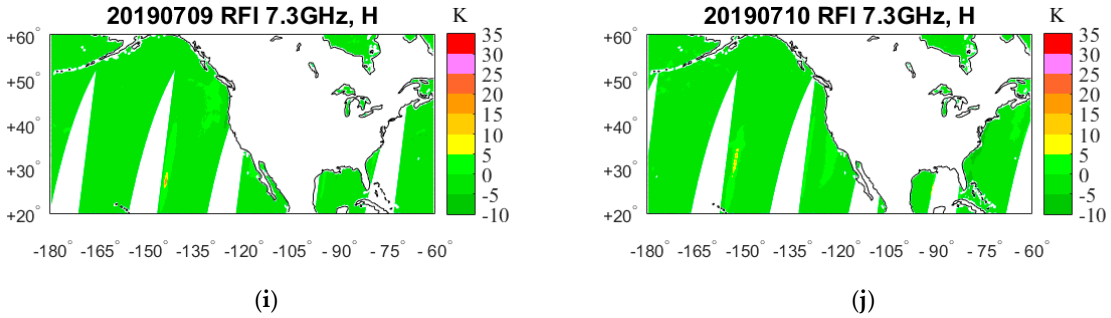

(**i**)

(**j**)

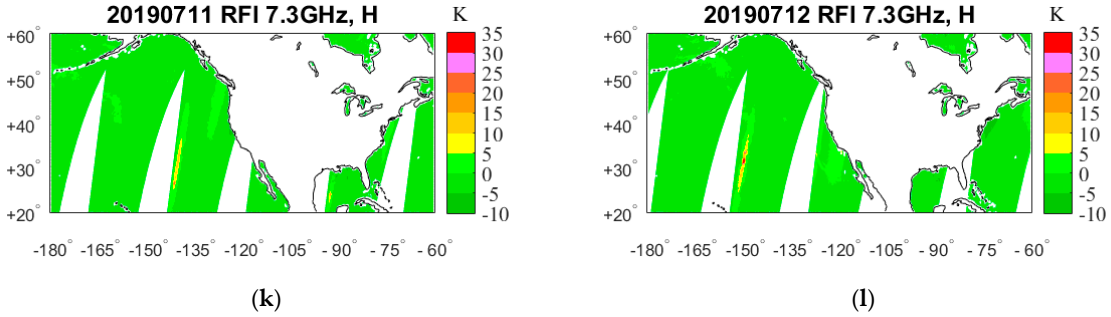

(**k**)

(**l**)

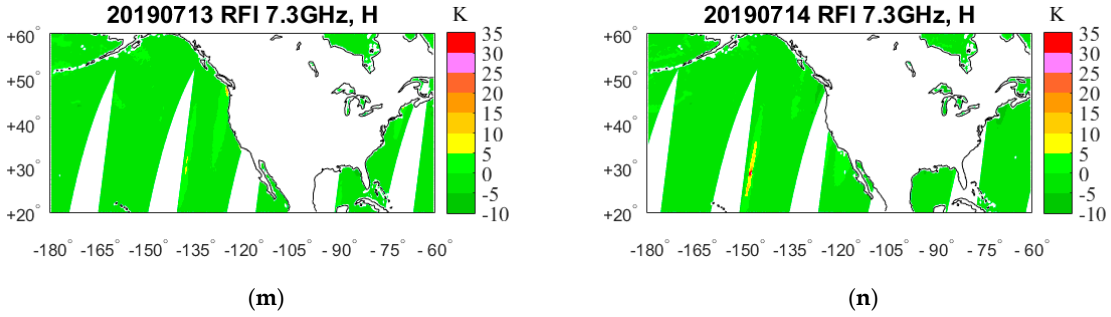

(**m**)

(**n**)

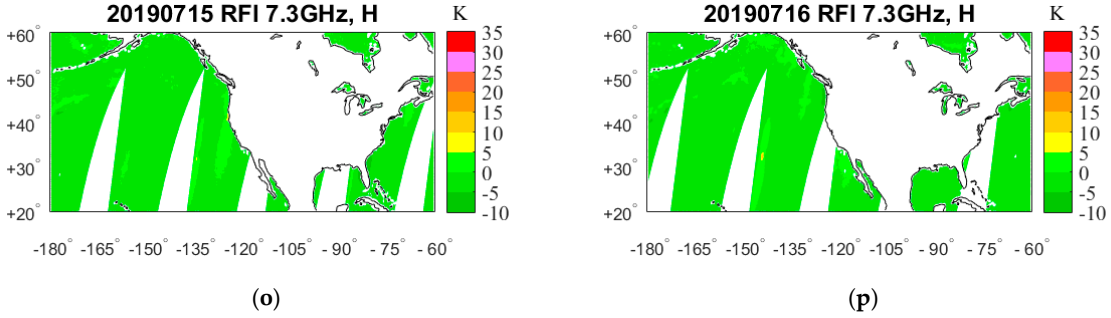

(**o**)

(**p**)

Figure 3. Spatial distribution of 7.3 GHz-H RFI, using GRDM over North American waters during the period 1–16 July 2019. (**a**) 1 July; (**b**) 2 July; (**c**) 3 July; (**d**) 4 July; (**e**) 5 July; (**f**) 6 July; (**g**) 7 July; (**h**) 8 July; (**i**) 9 July; (**j**) 10 July; (**k**) 11 July; (**l**) 12 July; (**m**) 13 July; (**n**) 14 July; (**o**) 15 July; (**p**) 16 July.

Figure 5 shows RFI signals in AMSR2 measurements for H-pol channels of 18.7 GHz over North American waters on 16 different days. RFI at 18.7 GHz are mainly present over the offshore marine areas of North America. The strongest RFI are distributed near the Great Lakes of America, and the RFI magnitude over the east and west coasts is stronger than that over the south coast. For example, waters in the vicinity of Los Angeles (1, 6, 8, 15 July), a swath of the east coast from New York to east of the Florida Peninsula (1, 3, 8, 10 July), the northwest coast of the Gulf of Mexico (1, 3, 5, 10, 12 July), from Seaside in the US to the west coast of Cumbria (2, 11 July), the Great Lakes (2, 4, 5, 7, 9, 11, 12, 13, 14, 16 July), the waters south of New Orleans (2, 7, 9, 11, 12, 14, 16 July), the waters west of Vancouver Island (3 July), the waters south of San Francisco (4, 13 July), the northeastern Gulf of Mexico (4, 11, 13 July), a swath of the eastern seaboard from Saint John in Canada to Beaufort in the US (5 July), the waters around the Florida Peninsula (6, 8, 15 July), the waters south of Vancouver Island (5, 7, 9, 12, 14, 16 July), from the Gulf of Maine on the east side of Boston to the east side of New York (7, 14 July), the Gulf of St. Lawrence to the south of the Nova Scotia Peninsula (9, 16 July), and the Wells–Oak Island east coast strip (12 July).

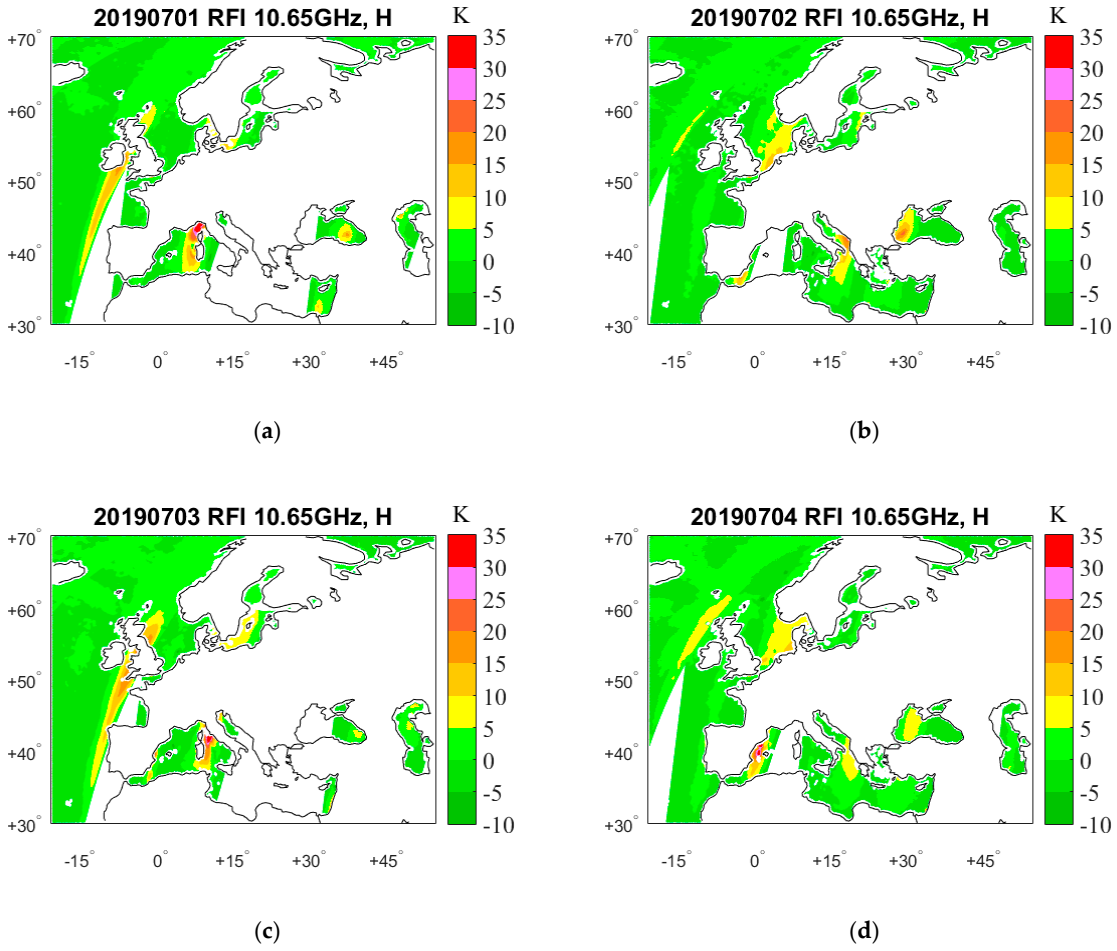

Figure 4. *Cont.*

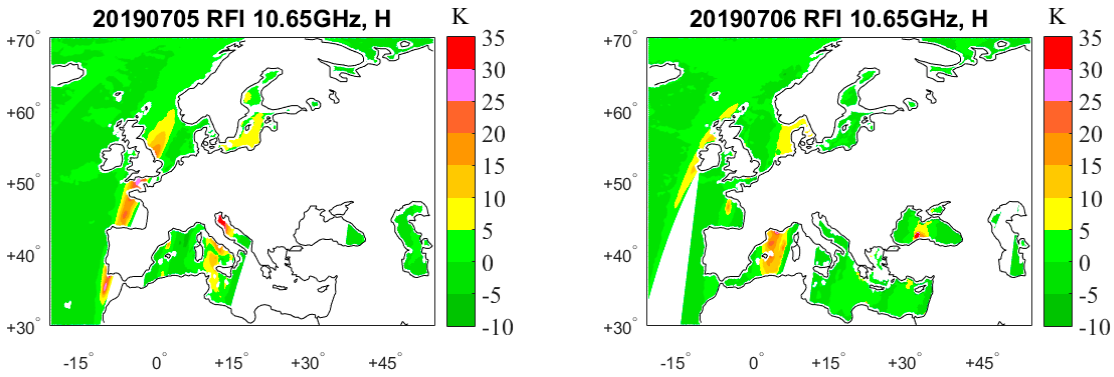

(**e**)

(**f**)

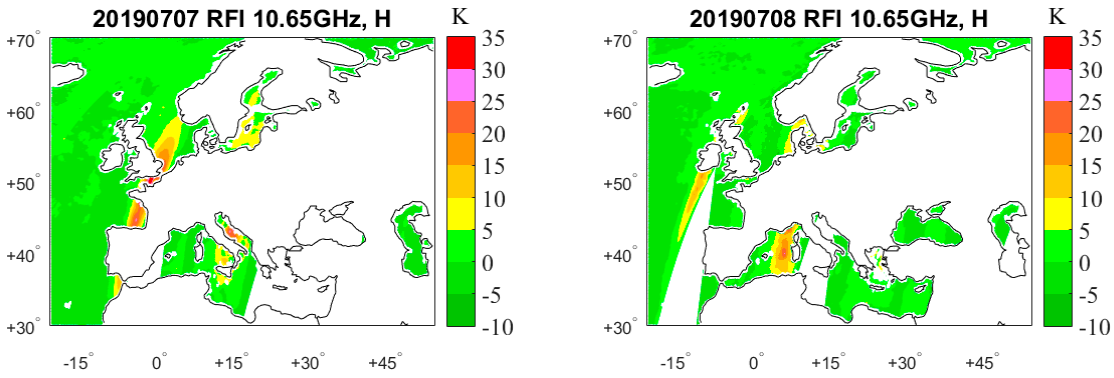

(**g**)

(**h**)

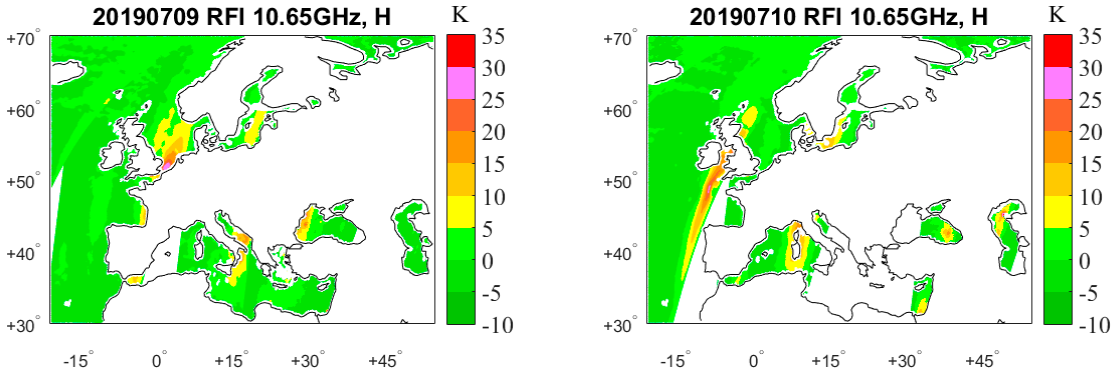

(**i**)

(**j**)

Figure 4. *Cont.*

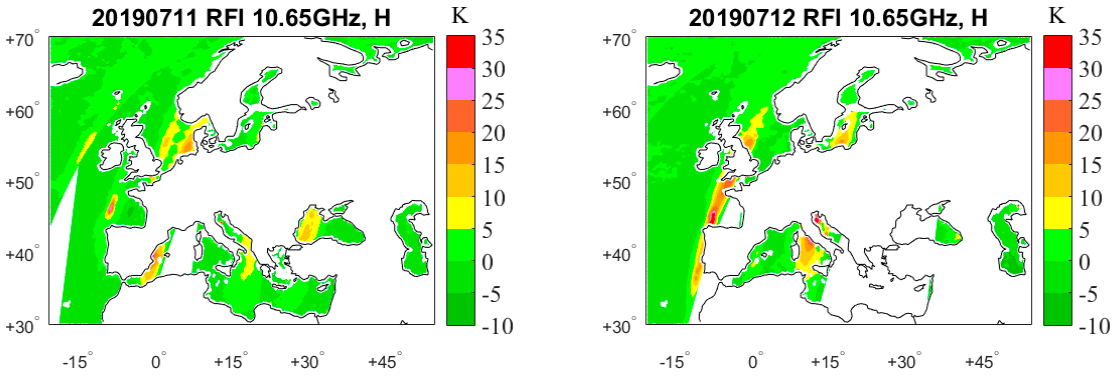

(**k**)

(**l**)

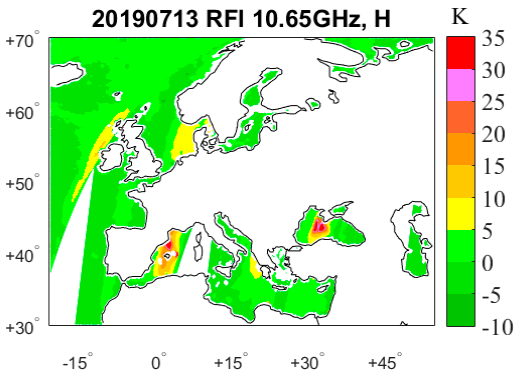

(**m**)

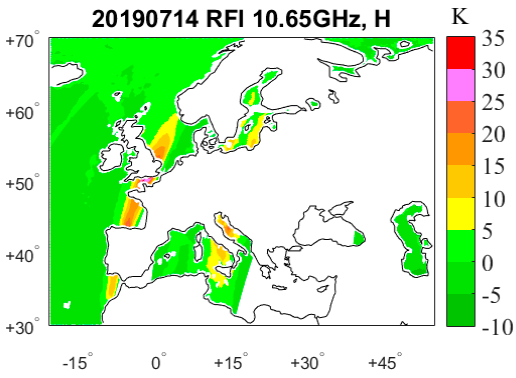

(**n**)

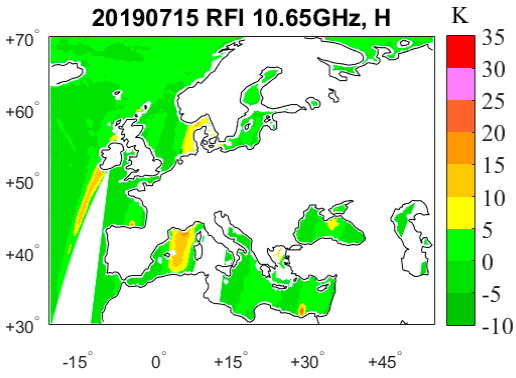

(**o**)

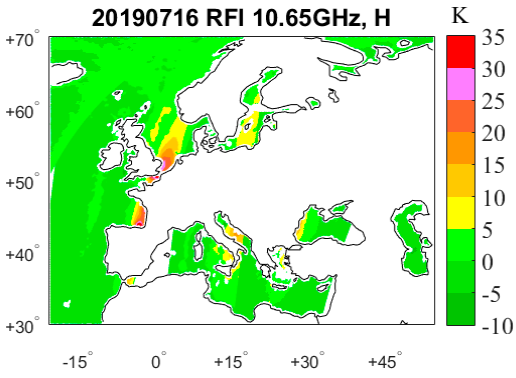

(**p**)

Figure 4. Spatial distribution of 10.65 GHz-H RFI, using GRDM over European waters during the period 1–16 July 2019. (**a**) 1 July; (**b**) 2 July; (**c**) 3 July; (**d**) 4 July; (**e**) 5 July; (**f**) 6 July; (**g**) 7 July; (**h**) 8 July; (**i**) 9 July; (**j**) 10 July; (**k**) 11 July; (**l**) 12 July; (**m**) 13 July; (**n**) 14 July; (**o**) 15 July; (**p**) 16 July.

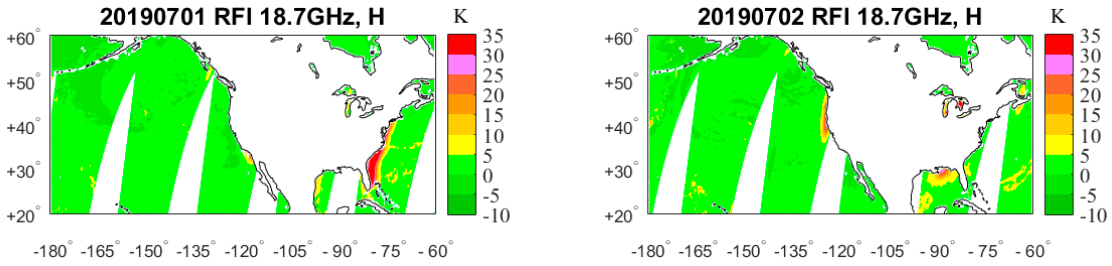

(**a**)

(**b**)

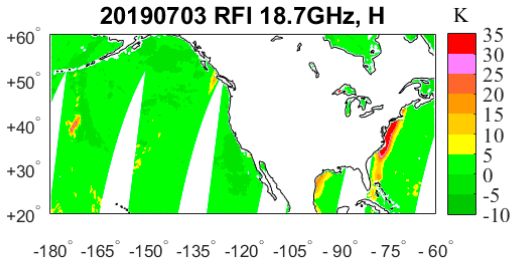

(**c**)

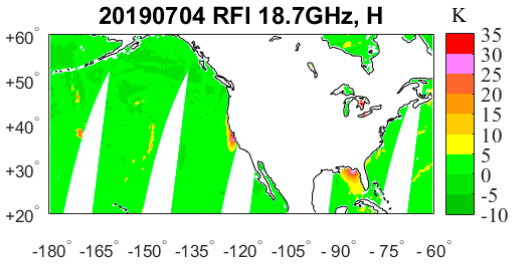

(**d**)

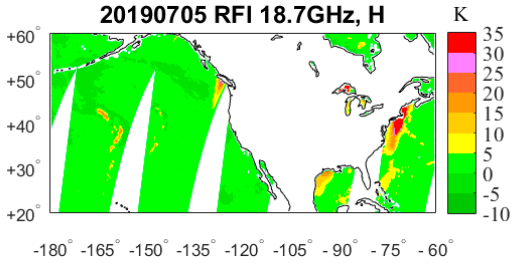

(**e**)

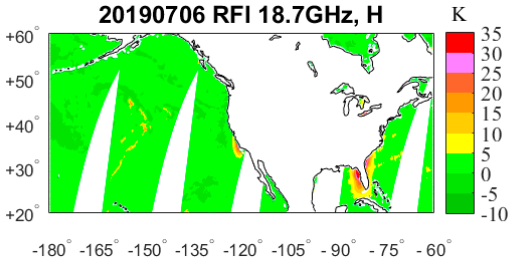

(**f**)

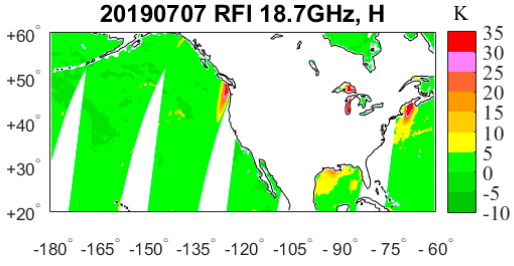

(**g**)

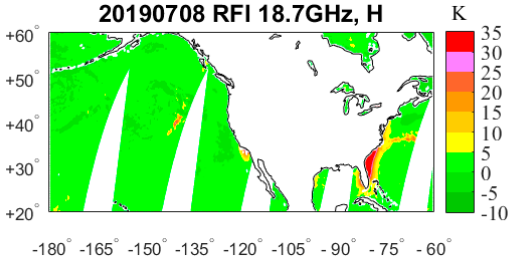

(**h**)

Figure 5. *Cont.*

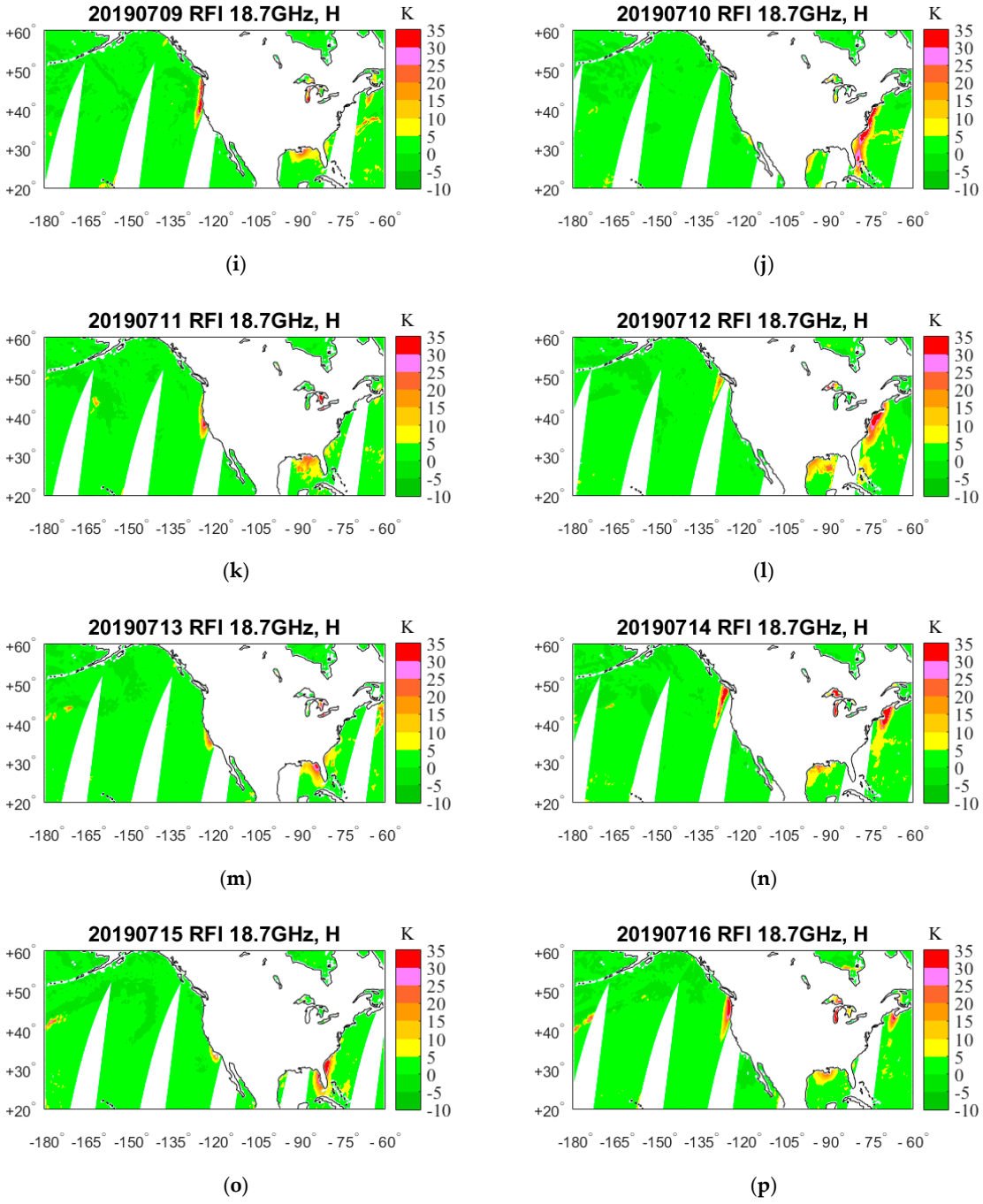

Figure 5. Spatial distribution of 18.7 GHz-H RFI, using GRDM over North American waters during the period 1–16 July 2019. (**a**) 1 July; (**b**) 2 July; (**c**) 3 July; (**d**) 4 July; (**e**) 5 July; (**f**) 6 July; (**g**) 7 July; (**h**) 8 July; (**i**) 9 July; (**j**) 10 July; (**k**) 11 July; (**l**) 12 July; (**m**) 13 July; (**n**) 14 July; (**o**) 15 July; (**p**) 16 July.

The results above show that the area of RFI coverage varies from day to day over the ocean, which is very different from that over the land. Figure 6 selects the spatial distribution of the RFI signals detected in H-pol and V-pol channels at 7.3 GHz, 10.65 GHz, and 18.7 GHz in typical areas. It can be seen that no matter which area is chosen, the RFI signals in H-pol channel are more widely distributed and stronger than those in V-pol channel. This is because the TB range of H-pol channel is much wider than that of V-pol channel, which also indicates that H-pol emissivity of different ground objects varies greater than those for vertical polarization [30].

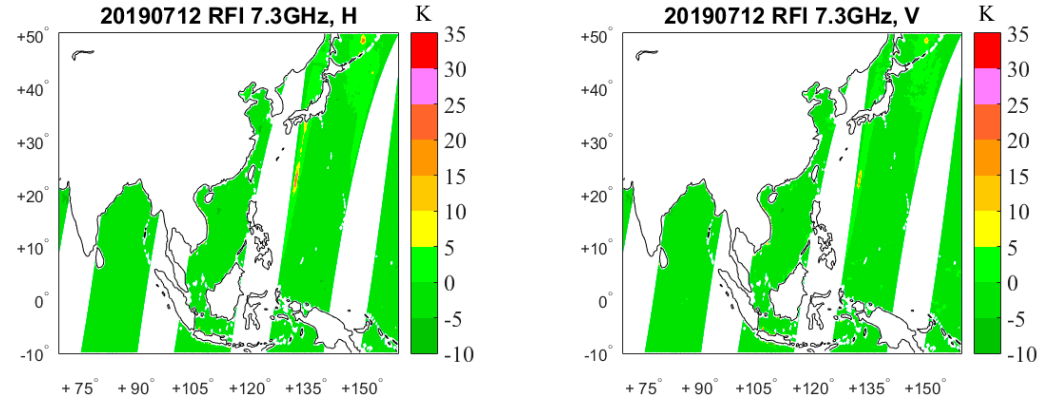

(**a**)

(**b**)

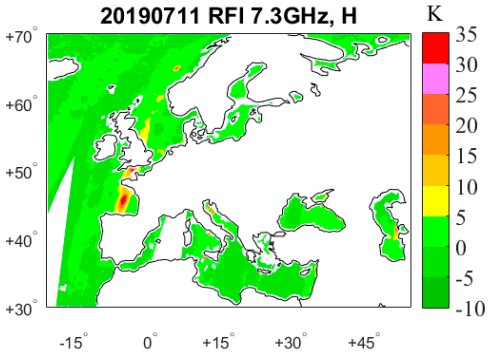

(**c**)

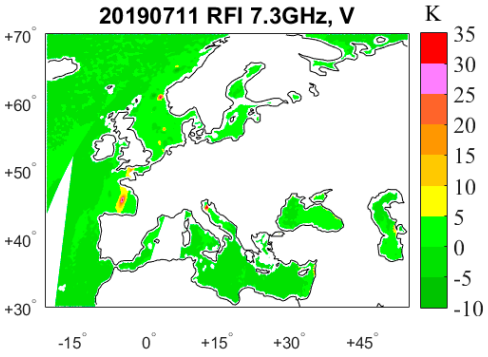

(**d**)

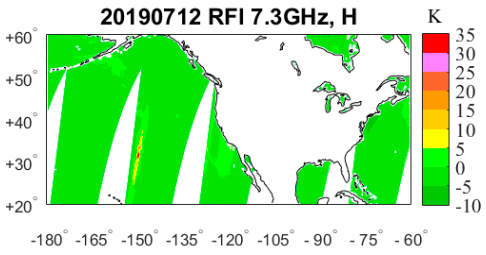

(**e**)

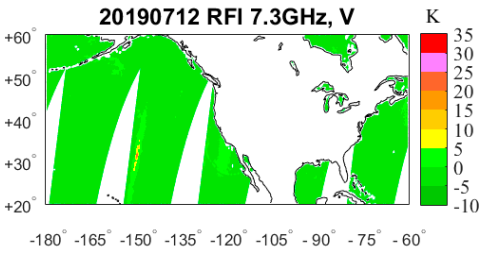

(**f**)

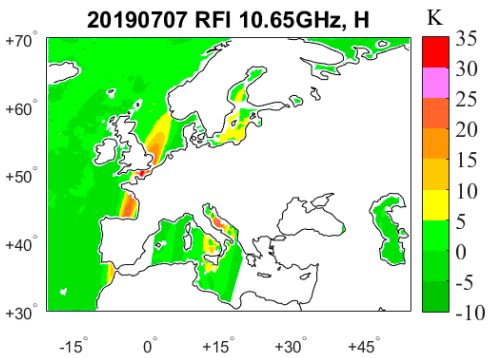

(**g**)

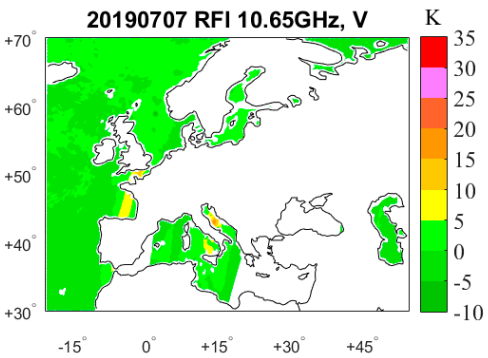

(**h**)

Figure 6. *Cont.*

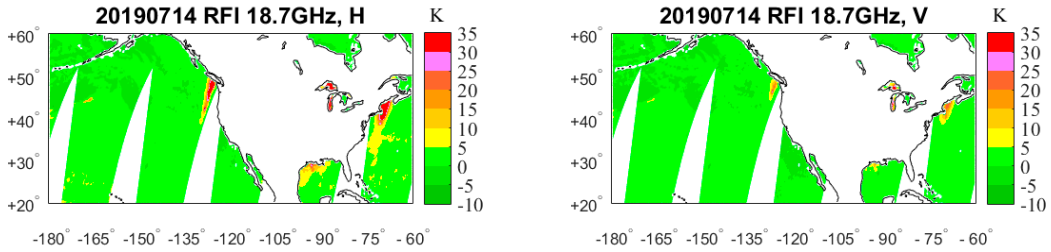

(**i**) (**j**)

Figure 6. Spatial distribution of RFI for H-pol (left panels) and V-pol (right panels), using GRDM. (**a**,**b**) 12 July; (**c**,**d**) 11 July; (**e**,**f**) 12 July; (**g**,**h**) 7 July; (**i**,**j**) 14 July.

In order to further evaluate the differences between the two polarization modes, the number of RFI-contaminated pixels each day during the 16-day period is showed in Table 2. Since the TB range of H-pol channel is much wider than that of V-pol channel, it can be seen that, under normal circumstances, the number of RFI signals in H-pol channel is more than that in V-pol channel of the same frequency, which is consistent with the conclusion drawn from Figure 6.

Table 2. Numbers of detected RFI pixels.

Numbers of Detected RFI Pixels										
Date (July)	7.3 GHz						10.65 GHz		18.7 GHz	
	Asia		Europe		USA		Europe		USA	
	H	V	H	V	H	V	H	V	H	V
1	1710	998	2191	990	32	22	10,307	1396	13,552	4220
2	1298	935	3196	840	1624	15	6779	1602	16,391	2654
3	3802	1466	2432	797	164	14	11,026	917	17,933	5282
4	3028	2012	4301	1068	2172	231	9846	1139	12,464	3009
5	1968	979	2349	923	54	25	11,065	3338	20,567	4796
6	1537	1288	3202	1020	553	48	9069	1723	11,734	3186
7	1574	1391	1987	884	1438	0	8101	1960	20,099	4100
8	2700	1258	2289	798	114	41	7793	1689	13,432	5183
9	1792	1476	2121	768	587	253	7270	1159	15,467	3049
10	1556	814	2175	1104	974	231	12,102	1318	16,075	6050
11	1339	1020	2655	1348	2176	465	8081	1487	13,472	3762
12	2478	1555	1080	473	2002	714	11,172	2518	21,415	5450
13	1169	1257	1914	592	526	92	9683	2219	14,263	4100
14	1622	1273	899	722	2180	662	9741	2426	18,790	4266
15	3062	1785	1496	657	122	19	8139	1257	11,077	3522
16	764	960	1615	709	281	80	7220	1919	16,783	4506

4.2. RFI Detection by DPCA

In this section, DPCA is used to identify the RFI signal in H-pol channel of AMSR2. Figure 7 shows the first PC coefficient (u_1) related to RFI in H-pol and V-pol channels of 7.3, 10.65, and 18.7 GHz corresponding to the typical regions in Figure 6. The first PCA step is performed on the TB data of the ten channels of AMSR2, and the TB matrix is reconstructed.

Taking $\alpha = 3$, divide the reconstructed TB field into the main part and the residual part, where the RFI signal is included in the residual part. Calculate the RFI index vector in Equation (11) for the separated TB data of the residual part, and then calculate the second PCA step to obtain the main component, namely the RFI signal. It can be seen from Figure 7 that the larger u_1 is, i.e., the warmer the tone area, the greater the probability of RFI and the stronger the intensity. In general, the area affected by the RFI detected by DPCA is similar to that detected by GRDM, and most of the RFI signals can be identified by the two methods.

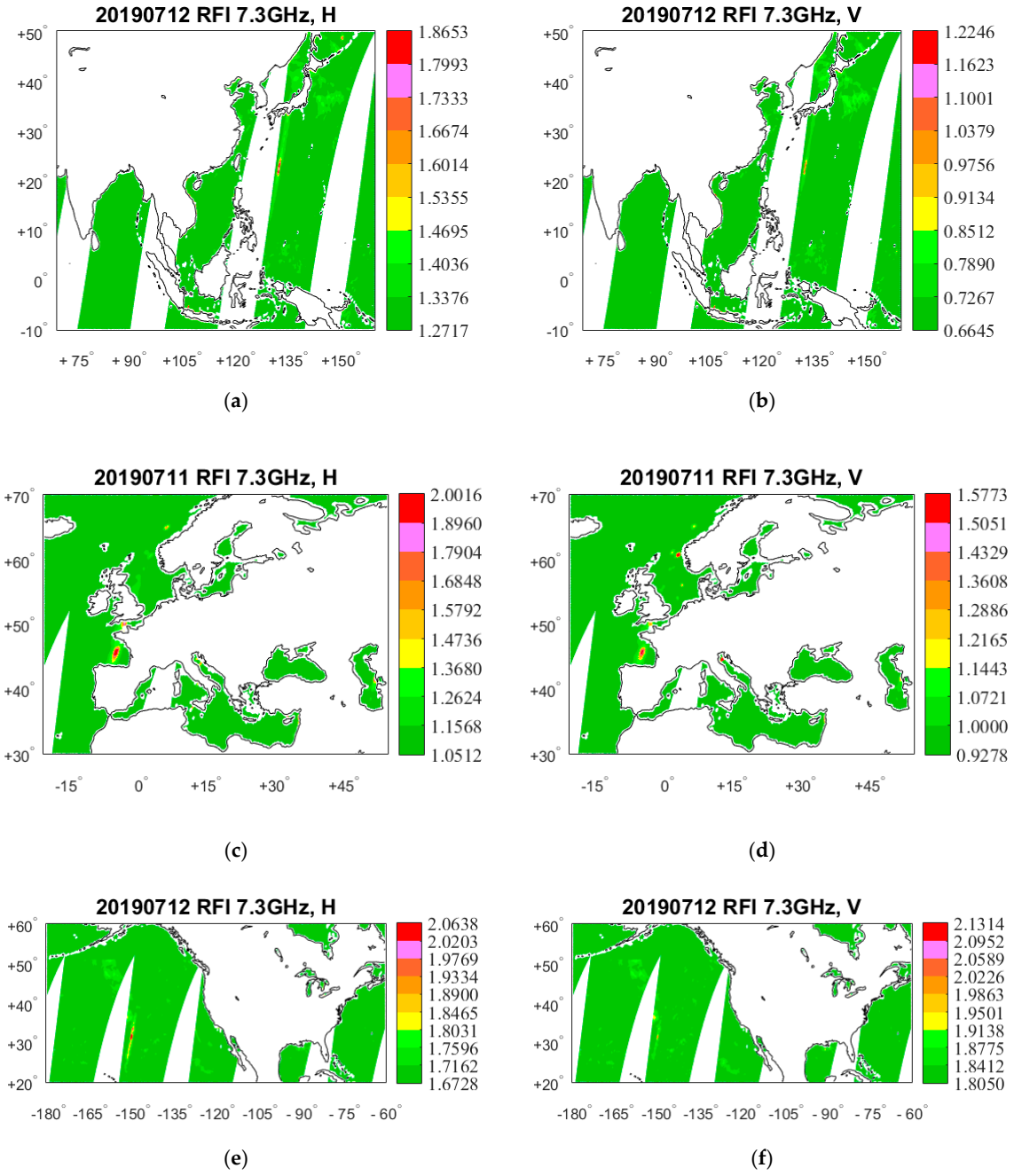

Figure 7. *Cont.*

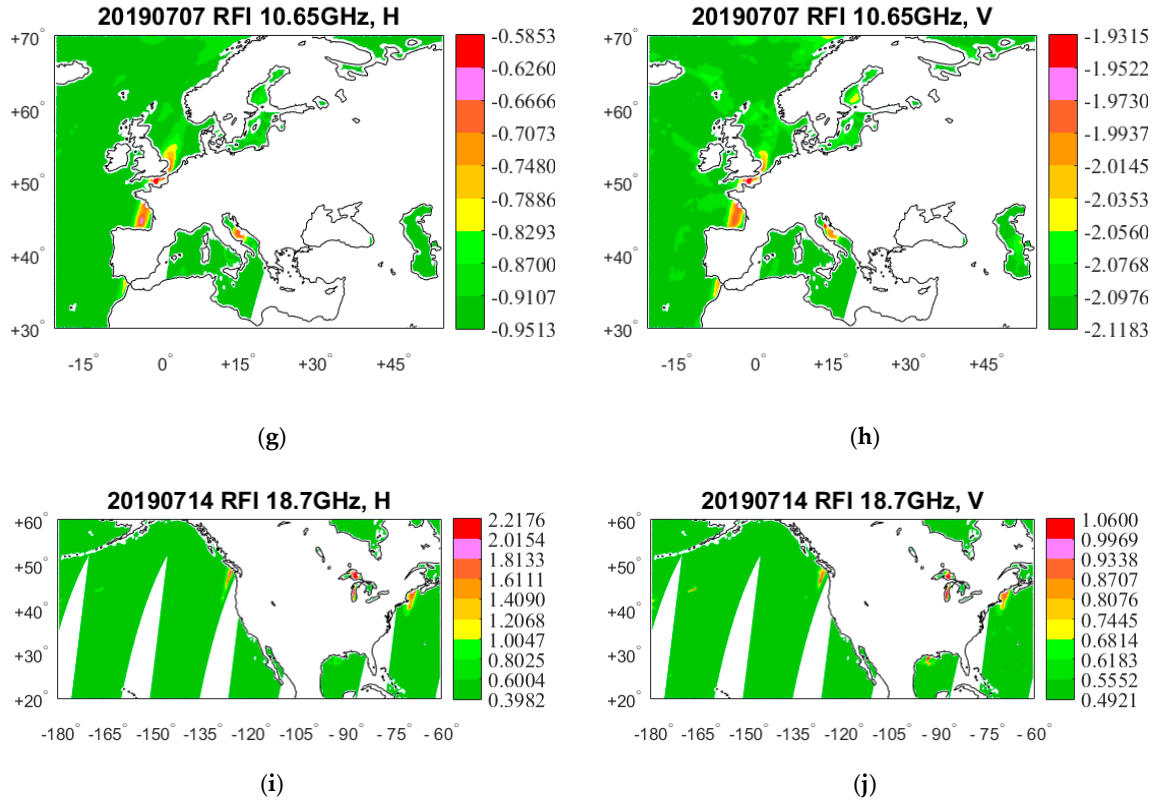

Figure 7. Spatial distribution of RFI for H-pol (left panels) and V-pol (right panels), using DPCA. (**a**,**b**) 12 July; (**c**,**d**) 11 July; (**e**,**f**) 12 July; (**g**,**h**) 7 July; (**i**,**j**) 14 July.

Figure 8 presents the scatterplots of the RFI signals obtained by the GRDM and observation TB in H-pol and V-pol channels corresponding to the various graphs in Figure 6. According to the scatter diagram, the TB range of H-pol channel is much wider than that of V-pol channel, which also indicates that H-pol polarization is more sensitive to the underlying surface than the vertical polarization. As can be seen from the scatter diagram distribution, the 7.3 GHz RFI signal with good strength over East Asian waters exists mainly in the TB range of 80–120 K in H-pol channel (with the value of ΔTB_H mostly between 5 and 30 K) and 170–200 K in V-pol channel (with the value of ΔTB_V mostly between 5 and 40 K). The strong RFI signals over European waters exist mainly in the TB range of 75–125 K in H-pol channel (with the value of ΔTB_H mostly between 5 and 40 K) and 160–190 K in V-pol channel (with the value of ΔTB_V mostly between 5 and 30 K). The strong RFI signals over North American waters exist mainly in the TB range of 80–90 K in H-pol channel (with the value of ΔTB_H mostly between 5 and 50 K) and 170–175 K in V-pol channel (with the value of ΔTB_V mostly between 5 and 30 K). The strong RFI signal of 10.65 GHz over European waters is present mainly in the TB range of 80–120 K in H-pol channel (with the value of ΔTB_H mostly between 5 and 35 K) and 170–190 K in V-pol channel (with the value of ΔTB_V mostly between 5 and 20 K). The strong RFI signal of 18.7 GHz over North American waters exists mainly in the TB range of 100–250 K in H-pol channel (with the value of ΔTB_H mostly between 5 and 50 K) and 180–250 K in V-pol channel (with the value of ΔTB_V mostly between 5 and 40 K). In addition, the generalized RFI index of H-pol channel is generally larger than that of V-pol channel, up to more than 50 K, indicating that the RFI signal of H-pol channel is stronger than that of V-pol channel. The latter is consistent with the information information provided in Table 2.

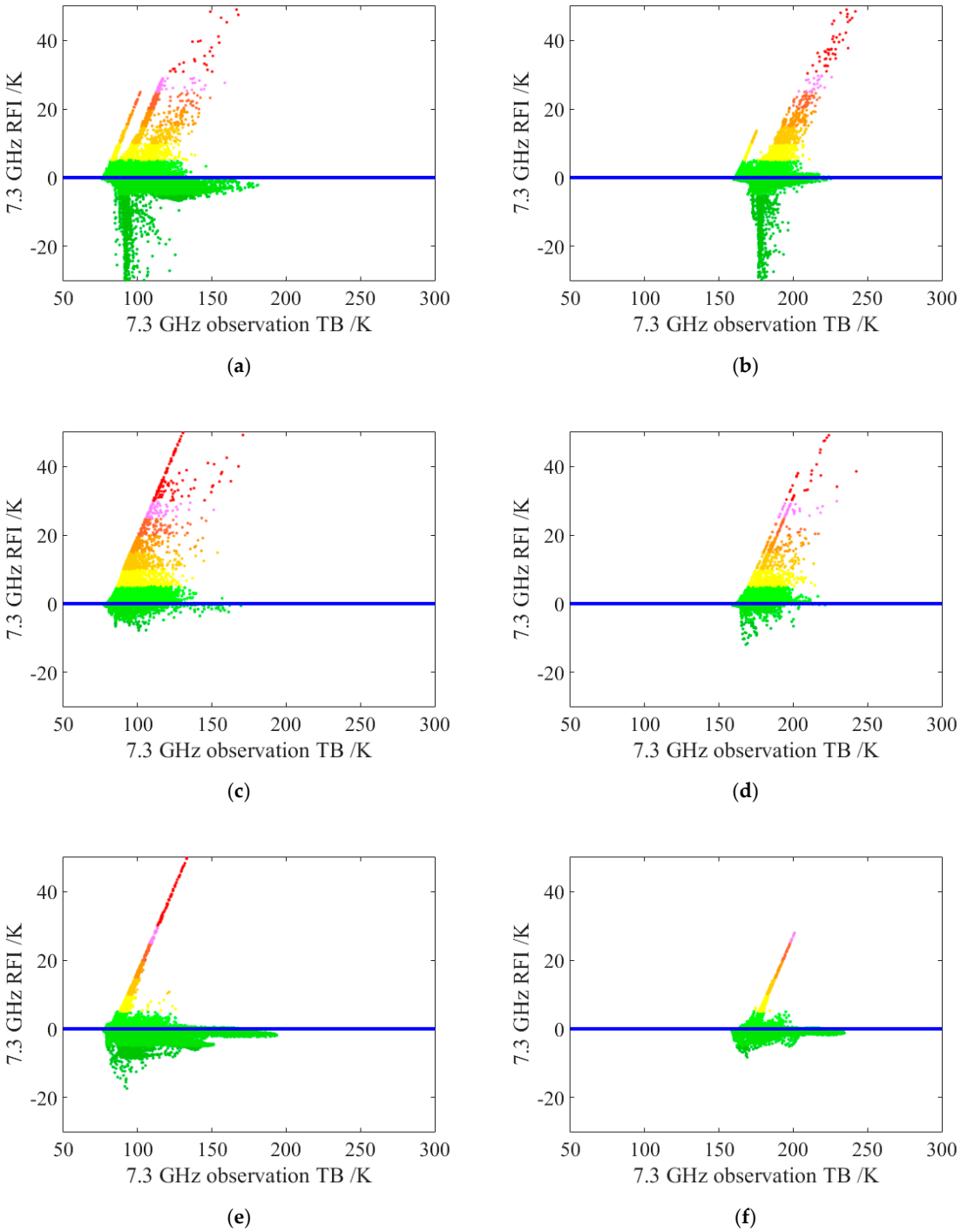

Figure 8. *Cont.*

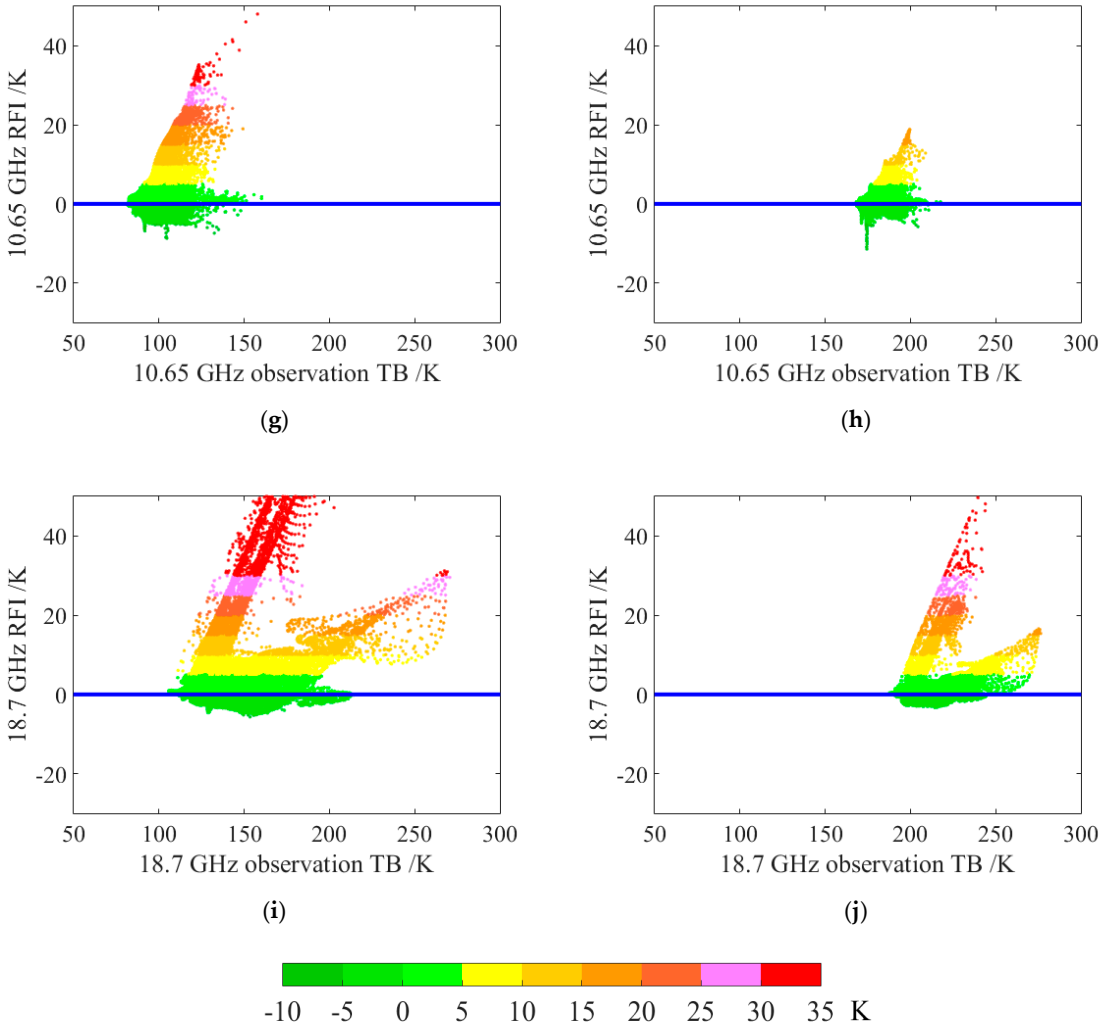

Figure 8. Scatter of RFI and observation TB for H-pol (left panels) and V-pol (right panels), using GRDM. (**a**,**b**) 12 July; (**c**,**d**) 11 July; (**e**,**f**) 12 July; (**g**,**h**) 7 July; (**i**,**j**) 14 July.

Figure 9. illustrates the scatterplots of DPCA u_1 and the 7.3 GHz H-pol and V-pol channel observed TB over East Asian, European and North American waters from 1 July to 16 July 2019; DPCA u_1 and 10.65 GHz H-pol and V-pol channel TB observation scatterplot over European waters; and DPCA u_1 and the 18.7 GHz H-pol and V-pol channel observation TB scatterplot over North American waters. It can be seen from the figure that, in the warm-toned area, the greater the probability and the stronger the intensity of RFI.

However, DPCA is only a qualitative RFI signal detection method, i.e., a large value of the coefficients of the first PC (u_1) of the residual data matrix $\boldsymbol{A}_2$ indicates the existence of RFI, and the larger the coefficient value of the first PC, the relative greater possibility of the existence of a strong RFI. Moreover, the ocean surface is not a completely smooth and flat mirror surface, especially when the ocean wind speed is high, and at the same time non-strict specular reflection causes the interference signal to have an angular spread. So, to effectively prevent a small-scale weather system from being mistaken for a false RFI signal, and to quantify RFI detection criteria using DPCA, the first PC coefficient $u_1 > u_{1\text{threshold}}$ and the generalized RFI index > 5 K are combined into a threshold criterion for judging whether there is RFI from a geostationary satellite. And the values of recognition thresholds ($u_{1\text{threshold}}$) in DPCA method developed for different channels are shown in Table 3.

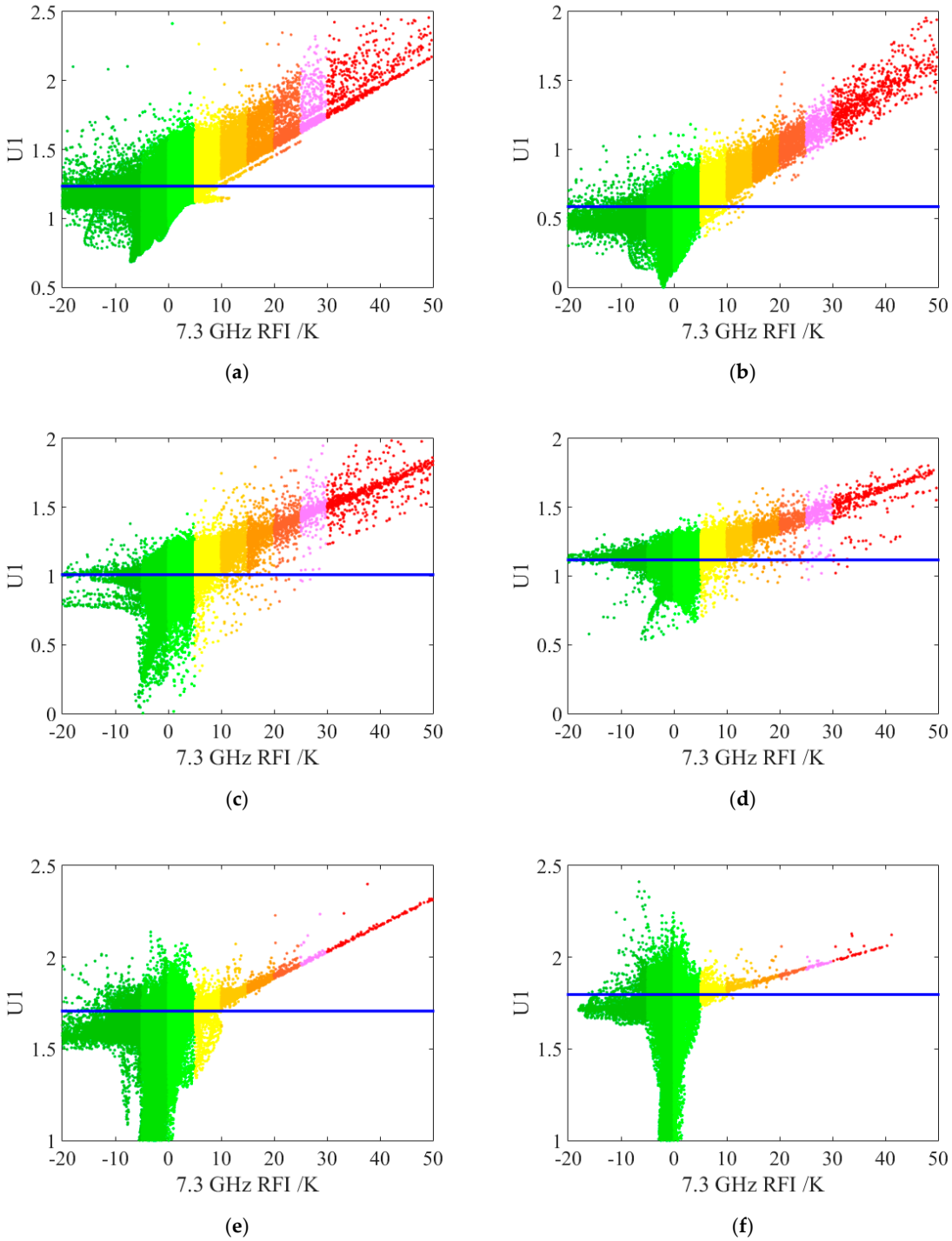

Figure 9. *Cont.*

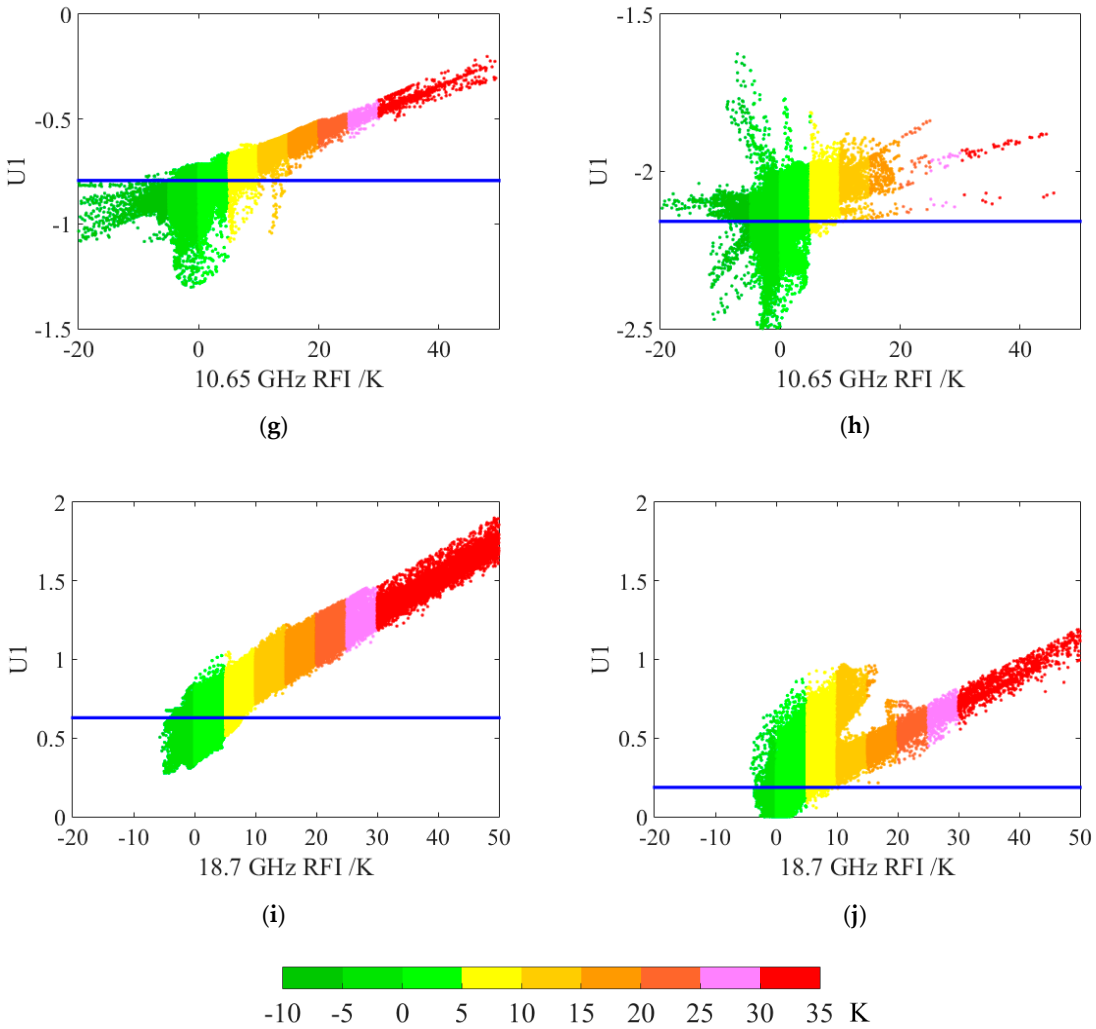

Figure 9. Scatterplots of DPCA u_1 and RFI index for H-pol (left panels) and V-pol (right panels) polarization using GRDM. (**a**,**b**) 7.3 GHz, Asia; (**c**,**d**) 7.3 GHz, Europe; (**e**,**f**) 7.3 GHz, USA; (**g**,**h**) 10.65 GHz, Europe; (**i**,**j**) 18.7 GHz, USA.

Table 3. Values of $u_{1\text{threshold}}$ for different channels.

	7.3 GHz						**10.65 GHz**		**18.7 GHz**	
	Asia		**Europe**		**USA**		**Europe**		**USA**	
	H	**V**	**H**	**V**	**H**	**V**	**H**	**V**	**H**	**V**
$U_{1\text{thres}}$	1.2336	0.5845	1.0098	1.1172	1.7063	1.7965	−0.7933	−2.1587	0.6293	0.1865

5. RFI Source Analysis

During the 16-day orbital period, the location and intensity of RFI signals over the ocean are changing every day. It also has been proved that, the RFI of any AMSR2 channel from the ocean surface only appears during descending orbit observation in the northern hemisphere, while no RFI signal appears during ascending orbit observation. When the wind speed on the ocean surface is small, specular reflection occurs. Communications/TV signals coming from stationary satellites are reflected by the ocean surface, which is the main sources of interference with the observations of satellite-borne passive microwave radiometers on the ocean [25]. Thus, the RFI location and intensity depend highly upon the relative geometric positions of the stationary satellite and the space-borne passive instrument.

Generally, stationary communication/TV satellites are fixed at a certain position over the Earth's equator and transmit signals continuously to designated areas [25,31]. Since the population density of coastal areas around the world is relatively high, static TV satellite antennas are designed to be directional and only intensively transmit to designated land areas. Although these geostationary satellite antennas are designed to focus on the land area, a small part of the strong radiation is still projected onto the ocean near the coastline, so there is a large-scale and strong RFI near the coastline [27]. In East Asia, Japan and other coastal areas have strong RFI. Over European waters, RFI signals are mainly distributed over the Mediterranean and other waters near Europe. Over North American waters, there are large-scale and strong RFIs near the coast, especially the east coast. Strong RFIs are also distributed over Lake Michigan, Lake Ontario, and Lake Erie of the Great Lakes. The closer to the inland, the stronger the RFI it becomes. The RFI is stronger over the north and west coasts, while the disturbance over the whole south coast is relatively weak.

In addition, AMSR2 C-band, X-band, and K-band channels have different RFI signal distribution areas over the ocean surface. This is caused by the different central frequencies currently used by the main stationary communication/TV satellites in different regions [27,32].

6. Conclusions

In this study, new coefficients which are applied to ocean surface were developed for a simplified GRDM. And the use of two independent identification methods is employed for cross-validation of the proposed technique, which allowed obtaining identification thresholds of the DPCA method. Meanwhile, the source and distribution characteristics of RFI over the ocean surface are analyzed. The results show that the proposed simplified GRDM works well over the ocean, which is a complement to the previous algorithm. Moreover, the detection results also show that the area of RFI coverage varies from day to day over the ocean, which is of big difference with that over the land. RFI signals over the waters are mainly distributed in Europe, East Asia, and North America, and the contaminated AMSR2 channels are in 7.3 GHz (C-band), 10.65 GHz (X-band), and 18.7 GHz (K-band). Moreover, RFI signals in H-pol channel are more widely distributed and stronger than those in V-pol channel of the same frequency. Furthermore, the generalized RFI index > 5 K and the first PC coefficient $u_1 > u_{1\text{threshold}}$ after residual matrix principal component analysis are used as the threshold criteria for cross-verification of RFI signals. In the absence of reliable data about radio signals over the ocean, cross-validation results obtained by different identification methods are helpful for identifying frequency interference in ocean data. In addition, AMSR2 suffers interference from geostationary satellites when observing the ocean surface in a descending orbit, while observation in the ascending orbit is not affected by such interference.

The cross-validation RFI detection method proposed in this study makes use of the correlation between channels of the microwave radiometer. It also does not require any other data or models and its calculation is relatively simple and straightforward. Therefore, it can be easily transplanted to RFI detection in existing or future space-borne microwave radiometer observations. However, the regression coefficients in this method were determined by selecting the observed TB data of the ocean surface excluding snow cover and sea ice cover over a period of time as training data. The applicability to snow cover and sea ice surface with obvious scattering effect remains to be further verified. Moreover, RFI Signal in a pixel may come from multiple geostationary satellites simultaneously. Considering the specific space position of geostationary satellites and the radiometer (AMSR2 in this study), an attempt can be made to calculate the correlation between them and the signal strength. Maybe we can do this as part of this study's continuation in the future is to investigate the specific location of the geostationary satellite of which the downlink signals frequency is around at 7.3 GHz over East Asia, Europe, and North America, so as to do further research. These are subjects of ongoing work in our group.

Author Contributions: Conceptualization: Y.W.; Methodology: Y.W.; Software: Y.W. and M.L.; Validation: Y.W. and M.L.; Formal analysis: Y.W., Y.B. and G.P.P.; Investigation: M.L.; Resources: Y.B.; Data curation: M.L.; Writing—original draft preparation: Y.W.; Writing—review and editing: Y.B. and G.P.P.; Visualization: M.L.; Supervision: Y.B.; Project administration: Y.B. All authors have read and agreed to the published version of the manuscript.

Funding: G.P.P.'s participation was supported financially by the European Union's Horizon 2020 Marie Skłodowska-Curie Project "ENViSIoN-EO" (grant agreement No 752094).

Acknowledgments: The numerical calculations in this paper have been done on the supercomputing system in the Supercomputing Center of Nanjing University of Information Science & Technology. We thank the anonymous reviewers for the comments that helped improve our manuscript.

Conflicts of Interest: The authors declare no conflict of interest.

References

1. Li, L.; Njoku, E.G.; Im, E.; Chang, P.S.; Germain, K.S. A preliminary survey of radio-frequency Interference over the U.S. in Aqua AMSR-E data. *IEEE Trans. Geosci. Remote Sens.* **2004**, *42*, 380–390. [CrossRef]
2. Njoku, E.G.; Ashcroft, P.; Chan, T.K.; Li, L. Global survey and statistics of Radio-Frequency Interference in AMSR-E land observations. *IEEE Trans. Geosci. Remote Sens.* **2005**, *43*, 938–947. [CrossRef]
3. Kidd, C. Radio frequency interference at passive microwave earth observation frequencies. *Int. J. Remote Sens.* **2006**, *27*, 3853–3865. [CrossRef]
4. Yang, H.; Weng, F. Error sources in remote sensing of microwave land surface emissivity. *IEEE Trans. Geosci. Remote Sens.* **2011**, *49*, 3437–3442. [CrossRef]
5. Wu, Y.; Weng, F. Applications of an AMSR-E RFI detection and correction algorithm in 1-DVAR over land. *J. Meteorol. Res.* **2014**, *28*, 645–655. [CrossRef]
6. Zou, X.; Zhao, J.; Weng, F.; Qin, Z. Detection of radio-frequency interference signal over land from FY-3B Microwave Radiation Imager (MWRI). *IEEE Trans. Geosci. Remote Sens.* **2012**, *40*, 4994–5003. [CrossRef]
7. Wu, Y.; Weng, F. Detection and correction of AMSR-E radio-frequency interference. *Acta Meteorol. Sin.* **2011**, *25*, 669–681. [CrossRef]
8. Lacava, T.; Coviello, I.; Faruolo, M.; Mazzeo, G.; Pergola, N.; Tramutoli, V. A multitemporal investigation of AMSR-E C-band radio-frequency interference. *IEEE Trans. Geosci. Remote Sens.* **2013**, *51*, 2007–2015. [CrossRef]
9. Wu, Y.; Qian, B.; Bao, Y.; Li, M.; Petropoulos, G.P.; Liu, X.; Li, L. Detection and analysis of c-band radio frequency interference in AMSR2 data over land. *Remote Sens.* **2019**, *11*, 1228. [CrossRef]
10. Du, J.; Kimball, J.; Shi, J.; Jones, L.; Wu, S.; Sun, R.; Yang, H. Inter-calibration of satellite passive microwave land observations from AMSR-E and AMSR2 using overlapping FY3B-MWRI sensor measurements. *Remote Sens.* **2014**, *6*, 8594–8616. [CrossRef]
11. Draper, D.W.; Newell, D.A.; Wentz, F.J.; Krimchansky, S. The Global Precipitation Measurement (GPM) Microwave Imager (GMI): Instrument overview and early on-orbit performance. *IEEE J. Sel. Top. Appl. Earth Obs. Remote Sens.* **2015**, *8*, 3452–3462. [CrossRef]
12. Ellingson, S.W.; Johnson, J.T. A polarimetric survey of radio-frequency interference in C-and X-bands in the continental United States using WindSat radiometry. *IEEE Trans. Geosci. Remote Sens.* **2006**, *44*, 540–548. [CrossRef]
13. Li, L.; Gaiser, P.W.; Bettenhausen, M.H.; Johnston, W. WindSat radio-frequency interference signature and its identification over land and ocean. *IEEE Trans. Geosci. Remote Sens.* **2006**, *44*, 530–539. [CrossRef]
14. Zhao, J.; Zou, X.; Weng, F. WindSat radio-frequency interference signature and its identification over Green land and Antarctic. *IEEE Trans. Geosci. Remote Sens.* **2013**, *51*, 4830–4839. [CrossRef]
15. Candy, B.; Saunders, R.W.; Ghent, D.; Bulgin, C.E. The impact of satellite-derived land surface temperatures on numerical weather prediction analyses and forecasts. *J. Geophys. Res. Atmos.* **2017**, *122*, 9783–9802. [CrossRef]
16. Al-Yaari, A.; Dayau, S.; Chipeaux, C.; Aluome, C.; Kruszewski, A.; Loustau, D.; Wigneron, J.P. The AQUI soil moisture network for satellite microwave remote sensing validation in south-eastern France. *Remote Sens.* **2018**, *10*, 1839. [CrossRef]
17. Du, J.; Kimball, J.; Reichle, R.; Jones, L.; Watts, J.; Kim, Y. Global satellite retrievals of the near-surface atmospheric vapor pressure deficit from AMSR-E and AMSR2. *Remote Sens.* **2018**, *10*, 1175. [CrossRef]
18. Pavelin, E.G.; Candy, B. Assimilation of surface-sensitive infrared radiances over land: Estimation of land surface temperature and emissivity. *Q. J. R. Meteorol. Soc.* **2014**, *140*, 1198–1208. [CrossRef]

19. Xie, Y.; Shi, J.; Lei, Y.; Li, Y. Modeling microwave emission from short vegetation-covered surfaces. *Remote Sens.* **2015**, *7*, 14099–14118. [CrossRef]
20. Grenkov, S.A.; Kol'tsov, N.E. Spectral-selective radiometer unit with radio-interference protection, radiophys. *Quantum Electron.* **2015**, *58*, 520–528.
21. Metelev, S.; Lvov, A. Estimation of the potential interference immunity of radio reception with spatial signal processing in multipath radio-communication channels. I. decameter range. *Radiophys. Quantum Electron.* **2016**, *59*, 329–340. [CrossRef]
22. Martin, G.M.; Milton, S.F.; Senior, C.A.; Brooks, M.E.; Ineson, S. Analysis and reduction of systematic errors through a seamless approach to modeling weather and climate. *J. Clim.* **2010**, *23*, 5933–5957. [CrossRef]
23. Berg, W.; Kroodsma, R.; Kummerow, C.; McKague, D. Fundamental climate data records of microwave brightness temperatures. *Remote Sens.* **2018**, *10*, 1306. [CrossRef]
24. Draper, D.; Newell, D. An assessment of radio-frequency interference using the GPM Microwave Imager. In Proceedings of the 2015 IEEE International Geoscience and Remote Sensing Symposium (IGARSS), Milan, Italy, 26–31 July 2015.
25. Adams, I.S.; Bettenhausen, M.H.; Gaiser, P.W.; Johnston, W. Identification of ocean-reflected radio-frequency interference using WindSat retrieval chi-square probability. *IEEE Geosci. Remote Sens. Lett.* **2010**, *7*, 406–410. [CrossRef]
26. Zabolotskikh, E.V.; Mitnik, L.M.; Chapron, B. Radio-frequency interference identification over oceans for C- and X-Band AMSR2 channels. *IEEE Geosci. Remote Sens. Lett.* **2015**, *12*, 1705–1709. [CrossRef]
27. Zou, X.; Tian, X.; Weng, F. Detection of television frequency interference with satellite microwave imager observations over oceans. *J. Atmos. Ocean. Technol.* **2014**, *31*, 2759–2776. [CrossRef]
28. Tian, X.; Zou, X. An empirical model for television frequency interference correction of AMSR2 data over ocean near the U.S. and Europe. *IEEE Trans. Geosci. Remote Sens.* **2016**, *54*, 3856–3867. [CrossRef]
29. Kachi, M.; Imaoka, K.; Fujii, H.; Shibata, A.; Kasahara, M.; Iida, Y.; Ito, N.; Nakagawa, K.; Shimoda, H. Status of GCOM-W1/AMSR2 development and science activities. In *Sensors, Systems, and Next-Generation Satellites XII*; International Society for Optics and Photonics: Bellingham, WA, USA, 2008. [CrossRef]
30. Weng, F.; Yan, B.; Grody, N.C. A microwave land emissivity model. *J. Geophys. Res.* **2001**, *106*, 20115–20123. [CrossRef]
31. Guan, L.; Zhang, S. Source analysis of spaceborne microwave radiometer interference over land. *Front. Earth Sci.* **2016**, *10*, 135–144. [CrossRef]
32. Radio Spectrum Allocation. Available online: https://www.fcc.gov/engineering-technology/policy-and-rules-division/general/radio-spectrum-allocation (accessed on 10 May 2020).